AGU
ADVANCING EARTH AND SPACE SCIENCE

JGR Atmospheres

Key Points:

- An international project is ongoing to elucidate the mechanism of interhemispheric coupling (IHC) in the middle atmosphere
- Gravity waves (GWs), which are thought to play a key role in IHC, were observed by a radar network and simulated by high-resolution global model
- Initial results suggest that not only GWs but also large-scale waves are important for the IHC mechanism

Supporting Information:

Supporting Information may be found in the online version of this article.

Correspondence to:

K. Sato,
kaoru@eps.s.u-tokyo.ac.jp

Interhemispheric Coupling Study by Observations and Modelling (ICSOM): Concept, Campaigns, and Initial Results

Kaoru Sato[1] [ID], **Yoshihiro Tomikawa[2,3,4]** [ID], **Masashi Kohma[1]** [ID], **Ryosuke Yasui[5]**, **Dai Koshin[1]** [ID], **Haruka Okui[1]** [ID], **Shingo Watanabe[6]** [ID], **Kazuyuki Miyazaki[7,8]** [ID], **Masaki Tsutsumi[2,3]** [ID], **Damian Murphy[9]**, **Chris Meek[10]** [ID], **Yufang Tian[11,12]**, **Manfred Ern[13]** [ID], **Gerd Baumgarten[14]**, **Jorge L. Chau[14]** [ID], **Xinzhao Chu[15]** [ID], **Richard Collins[16]** [ID], **Patrick J. Espy[17]** [ID], **Hiroyuki Hashiguchi[18]**, **Andrew J. Kavanagh[19]** [ID], **Ralph Latteck[14]** [ID], **Franz-Josef Lübken[14]** [ID], **Marco Milla[20]** [ID], **Satonori Nozawa[21]**, **Yasunobu Ogawa[2,3,4]** [ID], **Kazuo Shiokawa[21]** [ID], **M. Joan Alexander[22]** [ID], **Takuji Nakamura[2,3]** [ID], and **William E. Ward[23]** [ID]

[1]Department of Earth and Planetary Science, The University of Tokyo, Tokyo, Japan, [2]National Institute of Polar Research, Tachikawa, Japan, [3]Polar Science Program, Graduate Institute for Advanced Studies, SOKENDAI, Tachikawa, Japan, [4]Polar Environment Data Science Center, Research Organization of Information and Systems, Tachikawa, Japan, [5]Meteorological Research Institute, Japan Meteorological Agency, Tsukuba, Japan, [6]Japan Agency for Marine-Earth Science and Technology (JAMSTEC), Yokohama, Japan, [7]Jet Propulsion Laboratory, California Institute of Technology, Pasadena, CA, USA, [8]Joint Institute for Regional Earth System Science and Engineering, University of California, Los Angeles, Los Angeles, CA, USA, [9]Australian Antarctic Division, Kingston, TAS, Australia, [10]Institute of Space and Atmospheric Studies, University of Saskatchewan, Saskatoon, SK, Canada, [11]Key Laboratory of Middle Atmosphere and Global Environment Observation (LAGEO), Institute of Atmospheric Physics, Chinese Academy of Sciences, Beijing, China, [12]Xianghe Observatory of Whole Atmosphere, Institute of Atmospheric Physics, Chinese Academy of Sciences, Beijing, China, [13]Institut für Energie- und Klimaforschung–Stratosphäre (IEK–7), Forschungszentrum Jülich, Jülich, Germany, [14]Leibniz Institute of Atmospheric Physics, University of Rostock, Kühlungsborn, Germany, [15]Cooperative Institute of Research in Environmental Sciences & Department of Aerospace Engineering Sciences, University of Colorado Boulder, Boulder, CO, USA, [16]Geophysical Institute, University of Alaska Fairbanks, Fairbanks, AK, USA, [17]The Norwegian University of Science and Technology and Birkeland Centre for Space Science, Trondheim, Norway, [18]Research Institute for Sustainable Humanosphere, Kyoto University, Uji, Japan, [19]British Antarctic Survey, Cambridge, UK, [20]Seccion Electricidad y Electronica, Pontificia Universidad Catolica del Peru, Lima, Peru, [21]Institute for Space-Earth Environmental Research, Nagoya University, Nagoya, Japan, [22]NorthWest Research Associates, Boulder Office, Boulder, CO, USA, [23]Department of Physics, University of New Brunswick, Fredericton, NB, Canada

Abstract An international joint research project, entitled Interhemispheric Coupling Study by Observations and Modelling (ICSOM), is ongoing. In the late 2000s, an interesting form of interhemispheric coupling (IHC) was discovered: when warming occurs in the winter polar stratosphere, the upper mesosphere in the summer hemisphere also becomes warmer with a time lag of days. This IHC phenomenon is considered to be a coupling through processes in the middle atmosphere (i.e., stratosphere, mesosphere, and lower thermosphere). Several plausible mechanisms have been proposed so far, but they are still controversial. This is mainly because of the difficulty in observing and simulating gravity waves (GWs) at small scales, despite the important role they are known to play in middle atmosphere dynamics. In this project, by networking sparsely but globally distributed radars, mesospheric GWs have been simultaneously observed in seven boreal winters since 2015/16. We have succeeded in capturing five stratospheric sudden warming events and two polar vortex intensification events. This project also includes the development of a new data assimilation system to generate long-term reanalysis data for the whole middle atmosphere, and simulations by a state-of-the-art GW-permitting general circulation model using the reanalysis data as initial values. By analyzing data from these observations, data assimilation, and model simulation, comprehensive studies to investigate the mechanism of IHC are planned. This paper provides an overview of ICSOM, but even initial results suggest that not only GWs but also large-scale waves are important for the mechanism of the IHC.

Plain Language Summary In the late 2000s, an interesting form of the coupling between the Northern and Southern Hemispheres was discovered: when the winter polar stratosphere warms, the upper summer mesosphere also warms several days later. An international research project called Interhemispheric Coupling Study by Observations and Modelling (ICSOM) is ongoing to examine the mechanism of this interhemispheric coupling (IHC). This IHC phenomenon is thought to be the connection in the middle atmosphere (i.e., stratosphere, mesosphere, and lower thermosphere). Several promising mechanisms have

been proposed, but they remain controversial. This is because gravity waves (GWs) having small scales, which are difficult to observe and simulate, are thought to play a crucial role in the coupling. So, we have performed observations of GWs by networking radars over seven Northern Hemisphere winters, and succeeded in capturing five stratospheric warming events and two opposite events. We also developed a new data assimilation system for the entire middle atmosphere and used the global data produced by the system to simulate GWs with a high-resolution global model. By combining these research tools, we plan to elucidate the mechanism of IHC comprehensively. This paper presents an overview of ICSOM. Initial results show that not only GWs but also large-scale waves are important for the IHC mechanism.

1. Introduction

It is well known that when a stratospheric sudden warming (SSW) occurs in the polar regions, a cold anomaly in the winter polar mesosphere (e.g., Labitzke, 1972) and a warm anomaly in the middle and low latitudes of the stratosphere (e.g., Fritz & Soules, 1972) form a checkerboard pattern of temperature anomaly in the winter hemisphere. This checkerboard pattern is explained by the modulation of wave-induced meridional circulation in the stratosphere and mesosphere associated with the SSW (e.g., Körnich & Becker, 2010). Recent studies using atmospheric general circulation models (GCMs) covering the entire middle atmosphere, combined with satellite observations of polar mesospheric clouds, have reported that the effects of the SSW are not limited to the winter hemisphere but extend to the other hemisphere; specifically to the summer upper mesosphere and lower thermosphere (e.g., Becker & Fritts, 2006; Karlsson et al., 2007; Karlsson, McLandress, et al., 2009; Tan et al., 2012). Gumbel and Karlsson (2011) showed a clear negative correlation between the winter polar stratosphere temperature anomaly and the occurrence anomaly of the polar mesospheric clouds with a 7-day time lag. This observational fact implies a positive correlation in temperature between the winter stratosphere and the summer upper mesosphere. It has also been reported that this time lag in the coupling between the Northern and Southern Hemispheres depends on the season (Karlsson, Randall, et al., 2009).

Such a remote response is inferred to be caused by the modulation of the meridional circulation, driven by wave forcing and its interaction with the mean flow over the two hemispheres (e.g., Körnich & Becker, 2010; Murphy et al., 2012; Naren Athreyas et al., 2022; Yasui et al., 2021). Körnich and Becker (2010), hereafter referred to as KB10, proposed a simple and compelling scenario for the IHC and demonstrated it using an axisymmetric model that included gravity wave (GW) parameterizations. According to their scenario, first, the westerly polar night jet is significantly weakened or (in strong cases) reversed in association with the SSW. This change restricts the upward propagation of GWs having westward momentum fluxes into the mesosphere and facilitates the propagation of GWs with eastward momentum fluxes. The resultant weakening of the westward forcing caused by GW breaking/dissipation in the winter hemisphere upper mesosphere makes the Lagrangian poleward flow in the upper mesosphere weaker, the adiabatic heating/cooling response to which is a warm anomaly in the equatorial mesosphere and a cold anomaly in the polar mesosphere. The warm anomaly in the equatorial mesosphere weakens the latitudinal gradient of temperature in the summer mesosphere, which lowers the height of the weak wind layer above the summer hemisphere easterly jet and also lowers the location of the eastward forcing due to GWs. The equatorward Lagrangian circulation in the upper mesosphere of the summer hemisphere is then weakened, and the temperature in the upper mesosphere of the summer hemisphere increases. Therefore, the key physical driver in this scenario is the global modulation of mesospheric GWs.

However, there are a few important processes that are not taken into account in this scenario. Previous studies indicate that planetary waves such as quasi-two-day waves (QTDWs) are generated in-situ in the middle atmosphere due to for example, barotropic and/or baroclinic (BT/BC) instabilities and affect temperature in the summer polar upper mesosphere (e.g., France et al., 2018; Pendlebury, 2012; Siskind & McCormack, 2014). These dynamical instabilities can be caused by the redistribution of potential vorticity by inertial instability associated with planetary wave breaking in the winter hemisphere (e.g., Chandran et al., 2013; Lieberman et al., 2021; Orsolini et al., 1997) and also by momentum deposition due to the breaking and/or dissipation of GWs (e.g., Ern et al., 2013; Sato et al., 2018; Sato & Nomoto, 2015). In addition to the QTDWs, secondary GWs are important. The secondary GWs are generated in the middle atmosphere through an adjustment to the momentum deposited by primary GWs (Becker & Vadas, 2018; Vadas et al., 2018) and also by shear instability in the upper part of the summer easterly jet enhanced by primary GW forcing (Yasui et al., 2018, 2021).

Yasui et al. (2021) proposed a different scenario for the IHC. They indicated the importance of the equatorial stratosphere cold anomaly extending to the summer hemisphere middle latitudes, which is frequently observed

associated with a strong SSW. They analyzed outputs of simulations by a whole atmosphere model called the Ground-to-Topside Model of Atmosphere and Ionosphere for Aeronomy (GAIA; Jin et al., 2011) in which data is nudged to reanalysis data in the lower stratosphere and below so as to include realistic planetary waves in the stratosphere. They suggested that the mean zonal wind, modified by the latitudinally-elongated cold anomaly, enhances the in-situ generation of the QTDWs and GWs. These waves propagate upward and deposit westward momentum in the summer upper mesosphere and lower thermosphere causing a poleward flow anomaly there and a resultant warm anomaly in the polar region.

In contrast, Smith et al. (2020) argued that wave forcing in the summer hemisphere is not necessarily important for the IHC; the response in the summer hemisphere can be simply interpreted as the result of the mass circulation that develops to restore dynamical balance to the westward forcing caused by planetary wave breaking in the winter stratosphere. Furthermore, Smith et al. (2022) examined temperatures from Sounding of the Atmosphere using Broadband Emission Radiometry (SABER) onboard the Thermosphere Ionosphere Mesosphere Energetics and Dynamics (TIMED) satellite (Remsberg et al., 2008) and obtained results consistent with the mechanism proposed by Smith et al. (2020). They emphasized that IHC is a phenomenon having significant signals in the summer stratosphere as well as in the summer mesosphere. However, the observational results of Smith et al. (2022) do not rule out other possible IHC mechanisms, such as the contribution of GWs which are unresolved in the model as indicated by KH10 and Yasui et al. (2021). Therefore, further studies using high-resolution observations and GCM simulations which are able to capture GWs explicitly are required to elucidate the mechanism of the IHC.

For a comprehensive study of the IHC, a combination of various research tools is necessary. Mesosphere-stratosphere-troposphere (MST) radars (large-scale atmospheric radars) measure vertical profiles of three-dimensional wind vectors in the troposphere, stratosphere, and mesosphere with high temporal and vertical resolution, although there is an observational gap in the upper stratosphere and lower mesosphere (Hocking et al., 2016). An advantage of the MST radar observations is that they provide accurate estimates of the vertical flux of horizontal momentum associated with GWs. Meteor radars, Medium-Frequency (MF) radars, lidars, and airglow imagers are also capable of observing fluctuations associated with GWs in the mesosphere, although it is generally difficult to estimate the vertical momentum fluxes. In addition to high-resolution observations, state-of-the-art GCMs that have sufficiently high resolutions to express a significant spectral range of GWs explicitly in the whole neutral atmosphere extending to the turbopause located at a height of ~100 km (e.g., Becker & Fritts, 2006; Liu et al., 2014) are a valuable tool. In order to simulate the GW field at a certain time on a certain day, however, initial values of the whole neutral atmosphere are required. Reanalysis data produced by various meteorological organizations mainly span the atmosphere up to the lower or middle mesosphere, which is insufficient for the study of IHC because the upper mesosphere is expected to be a key region. Thus, a data assimilation system needs to be developed to produce reanalysis data for the whole neutral atmosphere. Validation of the reality of the simulated atmosphere using the high-resolution GCMs where the reanalysis data are given as initial conditions should be made with high-resolution observations such as from a radar network. On the other hand, the three-dimensional (3D) structure, global extent, and regionality of the disturbances detected by the observational instruments at respective locations can be examined using the verified model simulations. Moreover, quantitative studies of the atmospheric dynamics are possible using the model data which contains all required physical quantities. Thus, observations and model simulations are complementary. Each step of these developments requires considerable effort. We have established most of these research tools and now are in the phase of the full-scale IHC studies.

The questions that form the basis of the Interhemispheric Coupling Study by Observations and Modelling (ICSOM) international research project are:

1. How are the mean wind (in particular, the meridional component) and temperature at respective sites modulated by the SSW?
2. How are GW characteristics at respective sites modulated by the SSW?
3. How do the quasi-biennial oscillation and/or the semi-annual oscillation at the time of the SSW affect the IHC by modulating equatorial GWs?
4. Is the latitudinal variation of the modulated mean fields and wave fields consistent with theoretical expectations?
5. Are there any longitudinal variations of the modulated mean and wave fields?
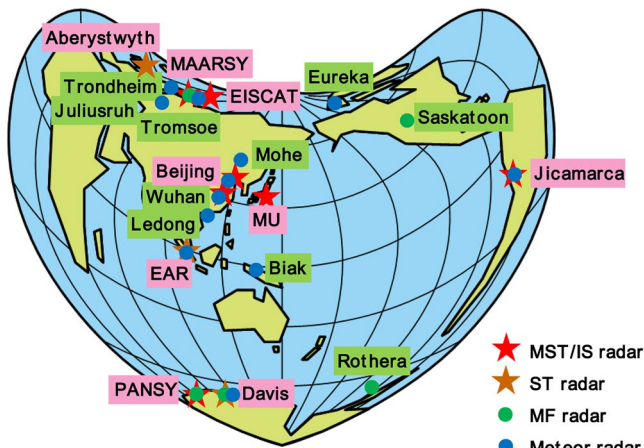
Figure 1. Interhemispheric Coupling Study by Observations and Modelling radar observation sites. MST/IS and ST radar locations are denoted by red and orange stars, respectively, and the radar name or site name is indicated by a pink plate. MF and meteor radar locations are denoted by green and blue circles, respectively, and the site name by a green plate.

6. Are high-resolution models able to successfully simulate variations of mean and wave (perturbation) fields observed at the respective ground-based observing sites? If so, how are the 3D structures of mean flow and temperature fields, and wave characteristics represented in these models? What dynamical processes cause such structures?

For ICSOM, we have conducted seven international joint observations in boreal winters since the first campaign in January–February 2016 when a minor but strong SSW event occurred. We have captured four major SSWs with various structures and timings in 2016/17, 2017/18, 2018/19, and 2020/21 and two vortex intensification (VI) events in 2019/20 and 2021/22 that are regarded as the opposite phenomenon of the SSW event. The data assimilation system, Japanese Atmospheric GCM for Upper Atmosphere Research (JAGUAR; Watanabe & Miyahara, 2009)-Data Assimilation System (JAGUAR-DAS; Koshin et al., 2020; Koshin, Sato, et al., 2022) has been developed to produce a long-term reanalysis data set for the whole neutral atmosphere up to a height of 105 km. Simulations of the hierarchical structure of phenomena and the variation of the whole neutral atmosphere, including GWs using a GW-permitting GCM, are currently in progress using the high-resolution JAGUAR model, in which the newly generated reanalysis data from JAGUAR-DAS are given as initial values. In this study, we describe the background characteristics of the phenomena captured during the seven joint observation periods, mainly using the radar and Aura Microwave Limb Sounder (MLS) (Schwartz et al., 2008; Waters et al., 2006) satellite observations and reanalysis data set. Initial results from a focused analysis of the major SSW event in the fourth campaign (ICSOM-4), whose onset was 1 January 2019, are shown, including GW variations during ICSOM-4 using SABER satellite data and model simulation outputs in the mesosphere.

Section 2 provides the configuration of the ICSOM project, including descriptions of the network of radars observing winds in the middle atmosphere and other complementary observation instruments, the data assimilation system and generated reanalysis data, and the GW-permitting GCM simulations. Section 3 gives rough description of the seven international observation campaigns. Section 4 shows initial observation results for each campaign regarding the time evolution of the mean field anomaly and radar observations of GWs and QTDWs. With a focus on ICSOM-4, time evolutions of dynamical fields including GW modulation associated with the SSW event revealed by reanalysis data, satellite observation and high-resolution modeling are highlighted in Section 5. Section 6 provides a summary and describes prospects of research.

2. ICSOM System Configuration: Instrumentation, Data Assimilation and Simulation

2.1. Radar Network for Mesosphere and Thermosphere Wind Measurements for ICSOM

Radar data used in the present study are obtained using three kinds of radar systems: MST radars, meteor radars, and MF radars. See Figure 1 for the locations and Table 1 for the details. We briefly describe each of the techniques in this section.

2.1.1. MST/IS Radars

MST radars are very high frequency (VHF) clear-air Doppler radars which measure wind velocity in a wide height region. The history of MST systems can be found in existing literature such as Hocking et al. (2016). These radars are usually large aperture array antenna systems with a narrow, steerable high gain antenna beam. They detect coherent echoes coming back from refractive index variations caused by atmospheric turbulence, which follows the motion of the ambient neutral atmosphere. The notable capability of these systems is the measurement of 3D wind velocity vectors with high temporal and vertical resolutions, especially the vertical component, which is enabled by the narrow antenna beam. With this, these systems can further estimate height profiles of momentum flux of atmospheric GWs more accurately than any other existing radar techniques, by using the method developed by Vincent and Reid (1983). Some MST radars have sufficient transmitting power and antenna aperture

Table 1
Atmospheric Radars Participating in Interhemispheric Coupling Study by Observations and Modelling Campaigns (ICSOM)

Facility	Type	Location	Latitude	Longitude	Frequency (MHz)	Peak power	Principal investigators	References
Eureka SKiYMET MWR	Meteor	Eureka, Nunavut, Canada	80°N	86.4°W	33.4	12 kW	A. Manson, C. Meek	Hall et al. (2002)
Svalbard MWR	Meteor	Longyearbyen, Svalbard, Norway	78.2°N	16.0°E	31	7.5 kW	M. Tsutsumi, C. Hall	Wannberg et al. (1997)
EISCAT ESR	IS	Longyearbyen, Svalbard, Norway	78.15°N	16.03°E	500	1 MW	Y. Ogawa, I. Haggstrom	Rishbeth and Williams (1985)
EISCAT UHF	IS	Tromsø, Troms og Finnmark, Norway	69.59°N	19.23°E	929.5	2 MW	Y. Ogawa, I. Haggstrom	
Tromsø MWR	Meteor	Tromsø, Troms og Finnmark, Norway	69.58°N	19.22°E	30.25	7.5 kW	M. Tsutsumi, C. Hall	Hall (2001)
Tromsø MFR	MF	Tromsø, Troms og Finnmark, Norway	69.58°N	19.22°E	2.78	50 kW	C. Hall, A. Manson, C. Meek, S. Nozawa	
MAARSY	MST/IS	Andenes, Andøya, Norway	69.30°N	16.04°E	53.5	800 kW	R. Latteck, J. Chau	Latteck et al. (2012)
Andenes MWR	Meteor	Andenes, Andøya, Norway	69.27°N	16.04°E	32.55	12 kW	R. Latteck, J. Chau	Jaen et al. (2022)
Saura MFR	MF	Andenes, Andøya, Norway	69.14°N	16.02°E	3.17	116 kW	R. Latteck, J. Chau	Renkwitz et al. (2018)
Trondheim MWR	Meteor	Trondheim, Trøndelag, Norway	63.4°N	10.5°E	34.21	30 kW	P. J. Espy	de Wit et al. (2015)
Juliusruh MWR	Meteor	Juliusruh, Mecklenburg-Vorpommern, Germany	54.6°N	13.4°E	32.55	12 kW	R. Latteck, J. Chau	Jaen et al. (2022)
Mohe MWR	Meteor	Mohe, Heilongjiang, China	53.5°N	122.3°E	38.9	20 kW	G. Li	Yu et al. (2013)
Aberystwyth	MST	Aberystwyth, Wales, United Kingdom	52.42°N	4.01°W	46.5	160 kW	NERC	Slater et al. (1991)
Saskatoon MFR	MF	Saskatoon, Saskatchewan, Canada	52°N	107°W	2.22	25 kW	A. Manson, C. Meek	Gregory et al. (1981)
Beijing MWR	Meteor	Beijing, China	40.3°N	116.2°E	38.9	7.5 kW	G. Li	Yu et al. (2013)
Beijing MST radar	MST	Xianghe, Hebei, China	39.75°N	116.97°E	50	172 kW	Y. Tian, D. Lü	Tian and Lü (2017)
MU Radar	MST/IS	Shigaraki, Shiga, Japan	34.85°N	136.10°E	46.5	1 MW	T. Tsuda	Fukao, Sato, et al. (1985), Fukao, Tsuda, et al. (1985b)
Wuhan MWR	Meteor	Wuhan, Hubei, China	30.5°N	114.6°E	38.9	7.5 kW/20 kW	G. Li	Yu et al. (2013)
Wuhan MST radar	MST	Chongyang, Hubei, China	29.51°N	104.13°E	53.8	172 kW	G. Chen	Qiao et al. (2020)
Ledong MWR	Meteor	Ledong, Hainan, China	18.4°N	109°E	38.9	20 kW	G. Li	Wang et al. (2019)
EAR	ST	Koto Tabang, West Sumatra, Indonesia	0.20°S	100.32°E	47.0	100 kW	T. Tsuda	Fukao et al. (2003)
Koto Tabang MWR	Meteor	Koto Tabang, West Sumatra, Indonesia	0.20°S	100.32°E	37.70	12 kW	T. Tsuda	Batubara et al. (2011)
Biak MWR	Meteor	Biak, West Papua, Indonesia	1.17°S	136.10°E	33.32	12 kW	T. Tsuda	
Jicamarca Radar	MST/IS	Lima, Peru	11.95°S	76.87°W	49.92	4 MW	M. Milla	Hysell et al. (2013); Lee et al. (2019)
JASMET	Meteor	Lima, Peru	11.95°S	76.87°W	50	100 kW	D. Scipion	
Rothera MFR	MF	Rothera Station, Antarctica	67.6°S	68.1°W	1.98	25 kW	A. J. Kavanagh, D. Fritts	Jarvis et al. (1999)
Davis MST Radar	MST	Davis Station, Antarctica	68.58°S	77.97°E	55.0	70 kW	D. Murphy	Morris et al. (2004)
Davis MWR	Meteor	Davis Station, Antarctica	68.58°S	77.97°E	33.2	7.5 kW	D. Murphy	Murphy (2017)
Davis MFR	MF	Davis Station, Antarctica	68.58°S	77.97°E	1.94	25 kW	D. Murphy	Murphy and Vincent (2000)
PANSY	MST/IS	Syowa Station, Antarctica	69.00°S	39.59°E	47.0	520 kW	K. Sato	Sato et al. (2014)
Syowa MFR	MF	Syowa Station, Antarctica	69.00°S	39.59°E	2.4	50 kW	M. Tsutsumi	Tsutsumi et al. (2001)

for even incoherent scatter (IS) echoes in the ionosphere. The PANSY radar is one such system (Hashimoto et al., 2019; Sato et al., 2014). Mesospheric observations by MST radars are limited to daytime when ionization by sunlight occurs. Interestingly, in polar regions, mesospheric observations over a long duration are possible in summer because of the midnight sun. The strong summer echoes are also considered to be related to the existence of noctilucent clouds (e.g., Hocking et al., 2016). In the case of the PANSY radar, continuous observation data has been obtained for about 50 days. Using the data, a broadband spectrum of wind fluctuations ranging from 8-min to 20-day periods, which is rare for the mesosphere, has been successfully obtained (Sato et al., 2017).

2.1.2. Meteor Radars

Radio meteor echo measurements started in the middle of 20th century, mostly for the purpose of astronomical applications. In subsequent decades, the techniques were more widely used for wind measurements in the upper mesosphere and lower thermosphere (e.g., Aso et al., 1979; Kaiser, 1953). The technique was revisited in the late 20th century for the measurements of atmospheric temperature, utilizing the decay time of meteor echo power (e.g., Hocking, 1999; Hocking & Hocking, 2002; Tsutsumi et al., 1994, 1996). In more recent years, a momentum-flux measurement technique has been introduced (e.g., Hocking, 2005). Stimulated by these new approaches, the atmospheric community now actively conducts world-wide meteor radar measurement using commercially available systems (e.g., Hocking et al., 2001; Holdsworth et al., 2004). As meteor echoes are detected regardless of the presence or absence of sunlight, meteor radar observations are possible both during the day and night. In the present study, we use horizontal wind data obtained by these radars with typical temporal and vertical resolution of 1 hr and 2 km, respectively.

2.1.3. MF Radars

MF radars provide another wind measurement technique in the mesosphere and lower thermosphere, which had been more widely used than meteor radars until recently. Most MF radars employ a spaced antenna configuration and estimate horizontal wind velocities based on a correlation analysis technique (e.g., Briggs, 1984). Although there are known problems for the measurement in the height region above around 90 km (e.g., Reid, 2015), the MF radar technique can still provide useful wind information in the mesosphere, especially in the lower mesosphere where meteor radar systems cannot estimate wind velocities due to the insufficient number of meteor echoes. There are also a few exceptionally large aperture MF radars which can steer a narrow antenna beam in multiple directions like VHF MST radars. The momentum flux estimation technique based on multiple beams was first proposed and tested using one of such large aperture MF radars (Reid & Vincent, 1987).

2.2. Other Complementary Observations

Aura MLS temperature and geopotential height data, version 5, level 2 (Schwartz et al., 2008; Waters et al., 2006) in the height region from $z = 9.4$ km (261 hPa) to 97 km (1×10^{-3} hPa) are also used to examine the mean and planetary-scale wave fields during the observation campaigns. Climatology was obtained using the data from 2 December 2004 to 15 March 2022 and anomalies from the climatology were examined. Note that the temperature data from Aura MLS have cold biases of ~1 K in the upper troposphere and of ~10 K in the mesopause (Medvedeva et al., 2014; Schwartz et al., 2008).

GW temperature variances estimated from SABER were also analyzed for comparison with radar observations and high-resolution GCM simulations. The SABER instrument was onboard the TIMED satellite launched in December 2001 and its measurements are still ongoing (Remsberg et al., 2008). GWs are designated as the remaining components after removing the zonal-mean background temperatures and fluctuations due to planetary waves having zonal wavenumber $s = 1-6$ with wave periods longer than about 1–2 days as well as tides (Ern et al., 2018). Detectable horizontal and vertical wavelengths by SABER are greater than ~100–200 and ~4 km, respectively. These resolutions are lower than those of radar observations and GCM simulations. However, since the GW spectra tend to have a universal shape which is proportional to a power of the wavenumber and frequency over a wide range (e.g., VanZandt, 1982), it is expected that GW variances calculated from different data sources will exhibit similar behavior even if the resolutions, or in other words, observational filters differ.

It should be noted here that MLS data are not used for the GW analysis, as the MLS vertical resolution varies strongly with height (Ern et al., 2022; Livesey et al., 2022), making MLS unsuitable for deriving GWs in the mesopause region. Furthermore, SABER data are not utilized for the mean field analysis. As SABER takes a

unique orbit and the local time of SABER measurements changes at an interval of about 60 days, posing difficulties in analyzing the intraseasonal variability of the mean field (See Appendix A in Koshin, Kohma, et al., 2022).

We also used data from the E-Region Wind Interferometer (ERWIN), a field widened Michelson interferometer, located at Eureka, Nu, Canada, which measures winds using Doppler shifts in isolated airglow emission lines (Kristoffersen et al., 2013). Although the data are not used in the present paper, observations of Optical Mesosphere Thermosphere Imagers (OMTIs) (Shiokawa et al., 1999), lidars (Baumgarten, 2010; Chu et al., 2011, 2022; Nozawa et al., 2014; Thurairajah, Collins, Harvey, Lieberman & Mizutani, 2010), and IS observations of the EISCAT radar (Rishbeth & Williams, 1985) also participate in ICSOM.

2.3. Reanalysis Data

This study also uses 3-hourly 3D winds, temperature, and geopotential height from the Modern-Era Retrospective Analysis for Research and Applications, version 2 (MERRA-2; Gelaro et al., 2017). The data are provided for 42 pressure levels from 1,000 to 0.1 hPa with latitude and longitude resolutions of 0.5° and 0.625°, respectively. The vertical grid spacing is ∼2 km in the upper stratosphere and lower mesosphere, increasing to ∼5 km near 80 km altitude. MERRA-2 assimilates ground-based and satellite radiance observations, including the stratospheric channels of the available Advanced Microwave Sounding Unit (AMSU-A) instruments and Aura MLS temperatures (above 5 hPa) and ozone.

2.4. Data Assimilation for the Whole Neutral Atmosphere

In order to study the variability of the whole middle atmosphere associated with SSW, global data up to about 100 km altitude, that is, up to the lower thermosphere, are needed. A data assimilation system JAGUAR-DAS has been developed that can produce such data (Koshin et al., 2020; Koshin, Sato, et al., 2022). This assimilation system employs the four-dimensional local ensemble transform Kalman filter (4D-LETKF) data assimilation system developed by Miyoshi and Yamane (2007) that can assimilate data with relatively low computational cost to produce long-term reanalysis data. This system uses a T42L124 version of the JAGUAR GCM with a top at 150 km in the lower thermosphere (Watanabe & Miyahara, 2009), and assimilates temperature data from MLS and SABER and radiance data from Special Sensor Microwave Imager/Sounder (SSMIS; Swadley et al., 2008). The vertical grid spacing of the model is about 1 km in the middle atmosphere up to 100 km. Model error covariances are estimated from 50-member ensembles. The output from JAGUAR-DAS is 6-hourly and has a horizontal grid spacing of 2.8125° in latitude and longitude. In the present study, reanalysis data from JAGUAR-DAS over 15 years from January 2005 to December 2019 are used. Note that intercomparison of the middle atmospheric analyses for the Northern Hemisphere winter in 2009–2010 has shown that JAGUAR-DAS provides zonal-mean zonal wind and temperature fields, diurnal and semidiurnal migrating solar tides, and traveling planetary waves which are comparable to other analysis data sets (McCormack et al., 2021).

It is worth noting that in the process of the data assimilation, artificial invisible forcing, which is often called increment, is added to produce a realistic time evolution of the atmosphere, including events such as SSW. This increment accounts for deficiencies in the numerical model, such as those in GW parameterizations. Recent studies have revealed that the distribution of GW forcing in the middle atmosphere is largely affected by lateral propagation (e.g., Amemiya & Sato, 2016; Sato et al., 2009, 2012; Senf & Achatz, 2011) and secondary generation (e.g., Becker & Vadas, 2018), which are not reflected in most GW parameterizations. These effects can be incorporated into the data assimilation as a part of the increment.

2.5. Simulations Using a High-Resolution GW Permitting General Circulation Model

We have also been performing simulations using a GW-permitting JAGUAR (T639L340) which can resolve small-scale waves having horizontal wavelengths greater than 60 km and a vertical grid spacing of 300 m (Okui et al., 2021; Watanabe et al., 2022). No GW parameterizations are used in this model. This high-resolution GCM is an extension of the Kanto model (Watanabe et al., 2008), which reproduces a realistic middle atmospheric field without GW parameterizations. The Kanto model simulations revealed important aspects of the GWs in the middle atmosphere, including the global distribution of GW energy and momentum fluxes and the significance of oblique propagation of GWs toward the jet by refraction and advection by the mean winds (Sato et al., 2009, 2012).

In the mesosphere in particular, the wave forcing caused by GWs propagating from the lower atmosphere significantly modifies the mean field causing shear instability and BT/BC instability that respectively generate secondary GWs and Rossby waves/Rossby-gravity waves (Sato et al., 2018; Watanabe et al., 2009; Yasui et al., 2018, 2021). The wave forcing caused by the primary GWs can also generate secondary GWs through spontaneous adjustment (Vadas et al., 2018). Thus, the utilization of the GW-permitting GCMs provides a significant opportunity to examine such complicated dynamical processes in the middle atmosphere in which both GWs and Rossby waves/Rossby-gravity waves equally play crucial roles.

However, in general, the model fields gradually shift away from reality as the time integration progresses. Thus, the whole time period was divided into consecutive periods of 4 days, and an independent model run was performed for each 4-day period using the GW-permitting JAGUAR in which the model is initialized using the JAGUAR-DAS reanalysis data. Each model run consists of 3-day spectral nudging and 4-day free runs. The output data from the 4-day free runs are analyzed. So far, ICSOM-3 (Watanabe et al., 2022) and ICSOM-4 (Okui et al., 2021) simulations have been completed, in which the spectral nudging was performed only for large-scale structures with total horizontal wavenumbers (n) lower than 42, while higher horizontal wavenumber components ($n = 43$–639) freely evolve. In the present study, we used outputs from a new ICSOM-4 simulation in which the 3-day spectral nudging was performed only for $n = 0$–15 components so as to make the GWs' amplitudes and phases more continuous between adjacent runs than the previous simulation by Okui et al. (2021). The ERA5 reanalysis data set (Hersbach et al., 2020) with a 0.25° horizontal resolution was used to constrain $n = 0$–15 components in the troposphere, where JAGUAR-DAS with T42 (2.8125°) horizontal resolution is less reliable (Watanabe et al., 2022). A preliminary analysis was performed to demonstrate the usability of the GW-permitting GCM simulations.

Figure 2 gives the comparison in the magnitude of GW fluctuations $\sqrt{\overline{u'^2 + v'^2}}$ in the time-height section between radar observations and the GW-permitting GCM simulations, where u and v are zonal and meridional winds, respectively. For the sake of strict comparison in Figure 2, we designated GWs the wind fluctuation components (′) having periods shorter than 1 day in which tidal waves are roughly removed by extracting temporal average over the whole period displayed in Figure 2 for each time of the day (see Yasui et al. (2016) for details) for both radar observations and model simulations. The average shown by the overline is made using a 1-day running mean. Note that all GWs are spontaneously generated and freely propagate in the model.

The left column shows the results for the troposphere and lower stratosphere. Note that observations in the high-altitude regions above 15 km at Aberystwyth may not be very reliable due to low signal-to-noise ratios, and only data with sufficiently high signal-to-noise ratios are plotted for Syowa Station. It seems that the time variation and vertical distribution of the simulated GW amplitudes are roughly consistent, in terms of the amplitude variations in the time scale of several days and the magnitude of the amplitudes itself.

The right column shows the result for the upper mesosphere. The time variation of the GW amplitudes is also roughly consistent between the radar observations and model simulations. For example, GWs are less active in 23–28 December 2018 in Wuhan, and less active around 5 and 13 January 2019 at Syowa Station. However, the correspondence is not very high compared with that for the troposphere and lower stratosphere. This is likely because the GW sources are far below the upper mesosphere. Accumulation of error in the GW propagation paths in the model simulation could result in the large departure of the horizontal location of the GW packets in the upper mesosphere from the real atmosphere. Thus, we need to evaluate the variation of GWs not at a particular site but an average over certain spatial and time regions. It is encouraging that the simulated amplitudes of strong GW packets are slightly larger than but almost comparable to the radar observations. This suggests that quantitative studies of the GW contribution to the IHC are possible using the model simulation data. It should be also noted that although the effects of GWs on the mean flow are described by quadratic quantities such as momentum fluxes, we compared the amplitudes of GWs between the radar observations and model simulations. This is because the accuracy of the radar observations is determined for the wind itself and not to the variance of GWs.

Figure 3 shows time-height sections of meridional (v', left) and vertical (w', right) wind fluctuations having total wavenumbers $n = 21$–639, which are considered mainly due to GWs, for the time period of 27 December 2018 to 4 January 2019 obtained by two adjacent runs by the GW-permitting JAGUAR for ICSOM-4 covering the log-pressure height range from 0 km (1,000 hPa) to 105 km ($\sim 3 \times 10^{-4}$ hPa). The time interval of the model outputs is 1 hr. Locations of respective figures are Eureka (80°N, 86°W), Beijing (40°N, 116°E), Kototabang
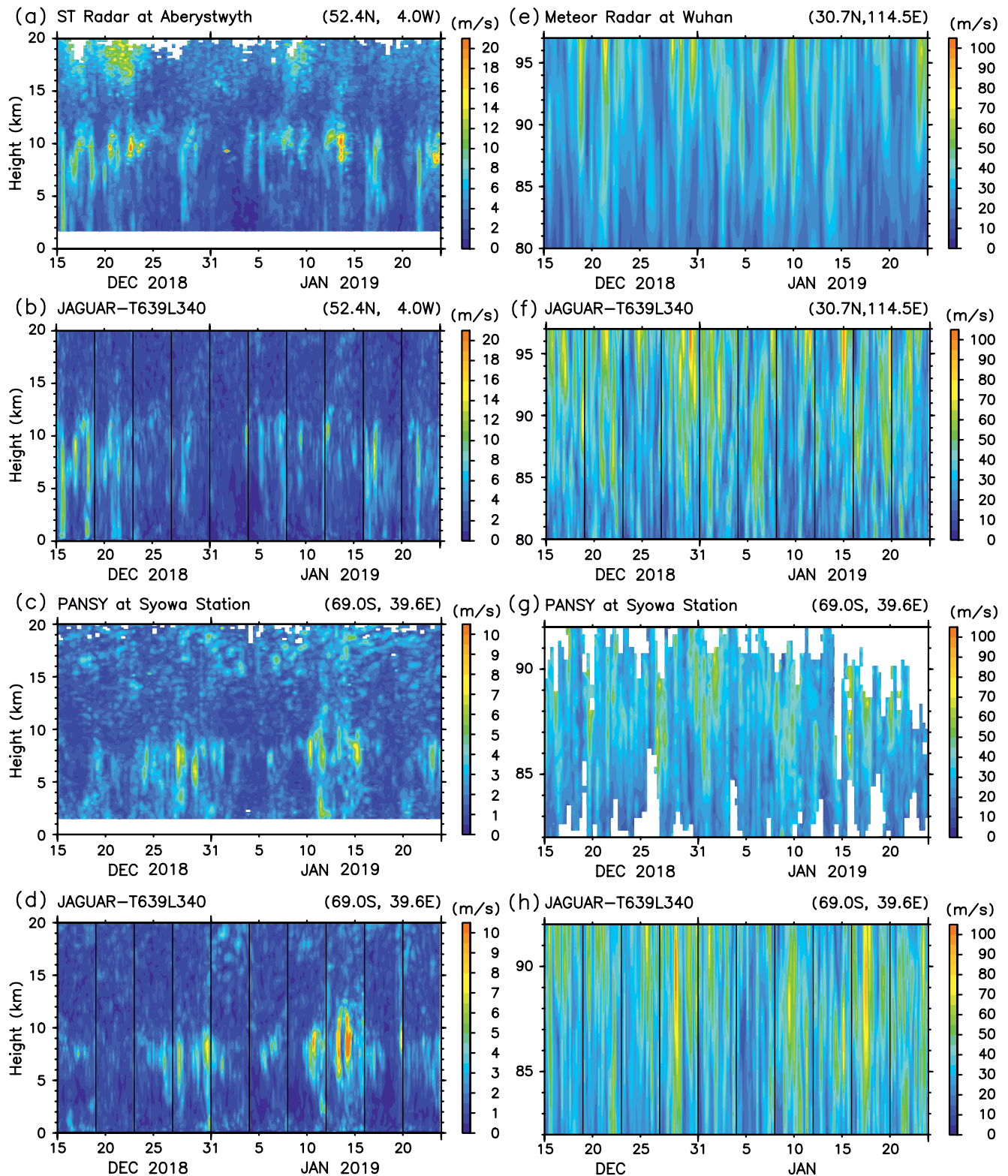
Figure 2. Time-height sections of the magnitude of gravity wave components from (a, c, e, g) radar observations and (b, d, f, h) the JAGUAR-T639L340 simulation at each station for ICSOM-4. The observations are from (a) the ST radar at Aberystwyth and (c) the MST radar (PANSY radar) at Syowa Station in the troposphere and lower stratosphere, and from (e) the meteor radar at Wuhan and (g) the PANSY radar at Syowa Station in the upper mesosphere. The model results at Wuhan (f) are lowpass filtered in the vertical with a cutoff wavelength of 4 km to match the radar vertical resolution of 2 km. Vertical lines for the model results represent the boundaries of the model runs. The vertical axes show the geometric height for radar observations and the geopotential height for model simulations.
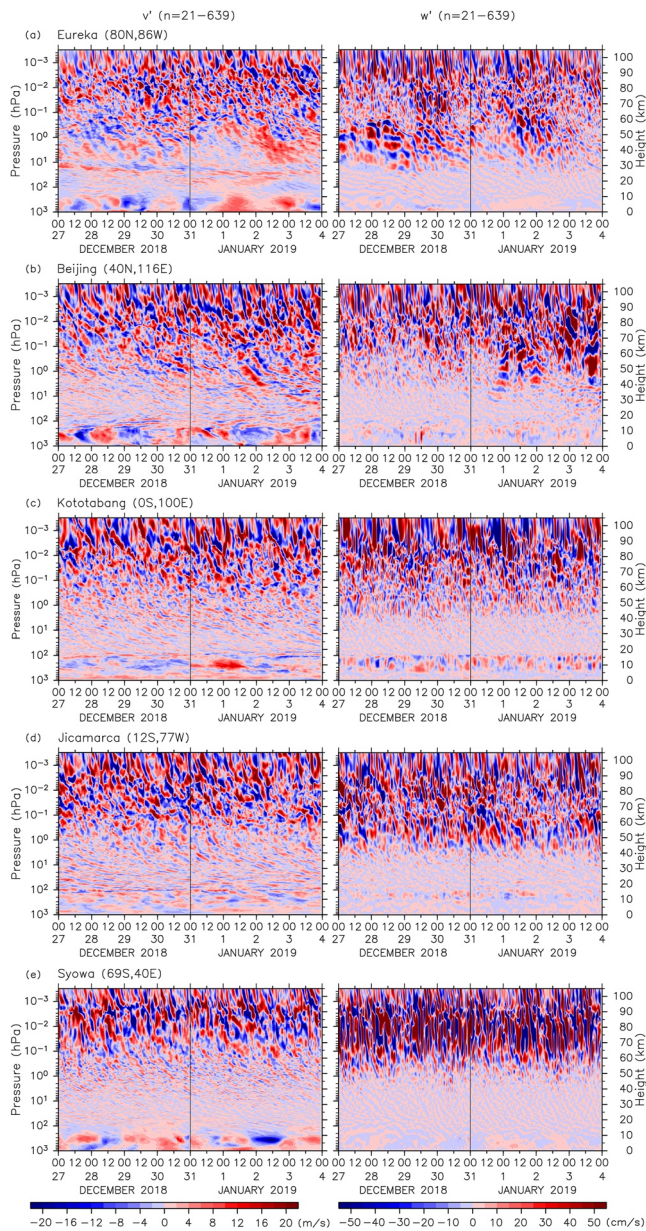
Figure 3. Time-height sections of meridional (left) and vertical (right) wind fluctuations associated with gravity waves from the high-resolution general circulation model simulation for ICSOM-4 at Eureka (80°N, 86°W), Beijing (40°N, 116°E), Kototabang (0°S, 100°E), Jicamarca (12°S, 77°W) and Syowa Station (69°S, 40°E) from the top. A vertical line of each section represents the boundary of the model runs.

(0°S, 100°E), Jicamarca (12°S, 77°W) and Syowa Station (69°S, 40°E) from the top. The thin vertical line denotes the boundary of the two runs for each section.

Note that the definition of GW fluctuations for Figure 3 is different from that for Figure 2, although both are applied to the same GW-permitting JAGUAR simulation outputs. The method for Figure 2 needs to be used for a strict comparison of the model simulation with radar observations. We utilized a different method for creating Figure 3 due to its direct removal of migrating tides, which cannot be applied to the radar observation time series.

For the v' component, in the stratosphere and mesosphere above $z = \sim 20$ km, downward phase propagation is dominant at all locations except for Eureka below $z = 30$ km. In contrast, in the troposphere below 200 hPa, strong long-period disturbances likely due to orographic GWs are observed at Eureka, Beijing, and Syowa Station. According to a linear theory, orographic GWs in steady background winds should have infinite ground-based wave periods. In the real atmosphere, however, their spatial phases are modulated due to slowly-varying background winds, resulting in the observation of long-period disturbances (e.g., Sato, 1990). At Eureka, an interesting long-lasting thin wavy structure is observed below $z = 30$ km over the whole displayed period. This feature is consistent with orographic GW behavior approaching the critical level which is located at $z = \sim 30$ km as shown later. Long-period disturbances are also observed at Kototabang and Jicamarca near the tropopause at $z = \sim 15$ km. This may be due to convective systems and/or equatorially-trapped waves.

It is interesting that the w' amplitudes in the mesosphere at Syowa Station are strongest among all stations shown in Figure 3. This feature may be related to low static stability in the upper mesosphere of the summer polar region which can enhance w' amplitudes of GWs for given momentum fluxes. It is also possible that GW activity is enhanced in the summer upper mesosphere through the in-situ generation of GWs in the middle atmosphere (e.g., Vadas et al., 2018; Yasui et al., 2018). Strong disturbances are also observed in Kototabang in the troposphere. This feature is likely due to convection in the equatorial region, but it should be noted that the w' component in the troposphere depends on the parameterization of cumulus convection used in the model, and hence comparison with observations should be made with caution in this region.

These model simulations of GWs in the middle atmosphere are not perfect in terms of the GW phases and amplitudes and strict locations of the GW packets, but still useful to examine GW behaviors in the IHC events. A significant advantage of GW-permitting model simulations is that the generation, propagation and dissipation of GWs are represented in a dynamically consistent manner: All GWs are spontaneously generated in the model. The model explicitly simulates GWs originating from the troposphere which are usually expressed by GW parameterizations in most climate models as well as those generated in-situ in the middle atmosphere. In addition, lateral propagation and refraction of GWs are also consistently simulated in the model. Okui et al. (2021) have demonstrated the advantage of the GW-permitting GCM for the study of the variability of the thermal structure in the mesosphere. A supplemental figure, Figure S1 in Supporting Information S1 displays the same time-height sections of v' and w' components as shown in Figure 3 but for other radar sites, including Longyearbyen (78°N, 16°E), Tromso (70°N, 19°E), Saskatoon (52°N, 107°W), Shigaraki (35°N, 136°E), Wuhan (30°N, 104°E), and Davis (69°S, 78°E).

Table 2
Main and Extended Observation Periods of Six Interhemispheric Coupling Study by Observations and Modelling (ICSOM) Campaigns

	Main observation periods	Extended periods	SSW onset
ICSOM-1	22 January–5 February 2016	6–16 February 2016	9 February 2016
ICSOM-2	22 January–5 February 2017	6–28 February 2017	1 February 2017
ICSOM-3	22–31 January 2018	1–28 February 2018	12 February 2018
ICSOM-4	22 December 2018–10 January 2019	11–20 January 2019	1 January 2019
ICSOM-6	30 December 2020–10 January 2021	11–20 January 2021	5 January 2021
			VI central date
ICSOM-5	12–21 January 2020	22–31 January 2020	31 January 2020
ICSOM-7	22–31 January 2022		2 February 2022

3. Description of Observation Campaigns

So far, seven campaigns have been conducted in January–February 2016 (ICSOM-1), January–February 2017 (ICSOM-2), January–February 2018 (ICSOM-3), December 2018–January 2019 (ICSOM-4), January–February 2020 (ICSOM-5), January–February 2021 (ICSOM-6), and January–February 2022 (ICSOM-7). Detailed campaign periods are summarized in Table 2. Each campaign was characterized by a relatively strong minor warming for ICSOM-1, a relatively weak major warming for ICSOM-2, strong major warmings for ICSOM-3, ICSOM-4, and ICSOM-6, and VI events for ICSOM-5 and ICSOM-7. The SSWs include both vortex displacement (ICSOM-1, -2, -4, -6) as well as vortex splitting (ICSOM-3) events. The major warming for ICSOM-4 and ICSOM-6 occurred in early January when the polar mesosphere summer echoes are strong. Thus, the PANSY radar, which is the largest MST radar in the Antarctic, could observe GWs continuously during the campaign periods. In this paper, a rough description of ICSOM-1 to ICSOM-7 is provided using data which are currently available.

Figure 4 shows polar stereo projection maps of potential vorticity at 845 K ($z = \sim30$ km) and geopotential height at 10 hPa ($z = \sim30$ km) from MERRA-2 on a key day of each campaign, namely a strong warming day for ICSOM-1, the major SSW onset day for ICSOM-2 to ICSOM-4, and ICSOM-6, and an intensified polar vortex day for ICSOM-5 and ICSOM-7. Movies S1–S7 and S8–S14 respectively visualize time evolutions of potential vorticity at 845 K and geopotential height at 10 hPa from 1 December to 15 March of the next year for ICSOM-1 to ICSOM-7. It seems that the strength of the warming of ICSOM-1 and ICSOM-2 is comparable. In ICSOM-3, the polar vortex was weakened and split into two. In ICSOM-4 and ICSOM-6, the polar vortex was displaced, significantly distorted, and dissipated after the onset.

4. Observational Results for Each Campaign

4.1. Time-Height Section of Anomaly of Zonal-Mean Temperature From MLS

The zonal-mean temperature fields are examined using data from Aura MLS. Figure 5 shows time-height sections of the zonal-mean temperature anomaly from the climatology for the Arctic (left column, an average for 65°N–82°N) and for the Antarctic (right column, 65°S–82°S) for each ICSOM campaign. The anomaly is a departure from the daily climatology that is calculated using data over 2 December to 15 March (of the next year) over 17 years from 2004 to 2021. The center on the horizontal axis represents the key day (i.e., the event onset). For ICSOM-5 and ICSOM-7, a temperature minimum day, 1 February 2020 and 2 February 2022 was used as the key day as there is no clear definition of the VI event.

Positive temperature anomalies associated with the SSW are seen at altitudes of 20–50 km in the stratosphere around the onset day. The positive anomalies accompany negative anomalies at altitudes of 50–80 km in the mesosphere. The positive anomalies and the negative ones above are particularly strong and long lasting in ICSOM-4. The positive anomalies descend to around the tropopause located at $z = \sim10$ km and continued until 26 January 2019. Another positive temperature anomaly is seen in ICSOM-4 at altitudes of 70–90 km after 31 December 2018, corresponding to the mesospheric inversion layer and the elevated stratopause (Okui et al., 2021).
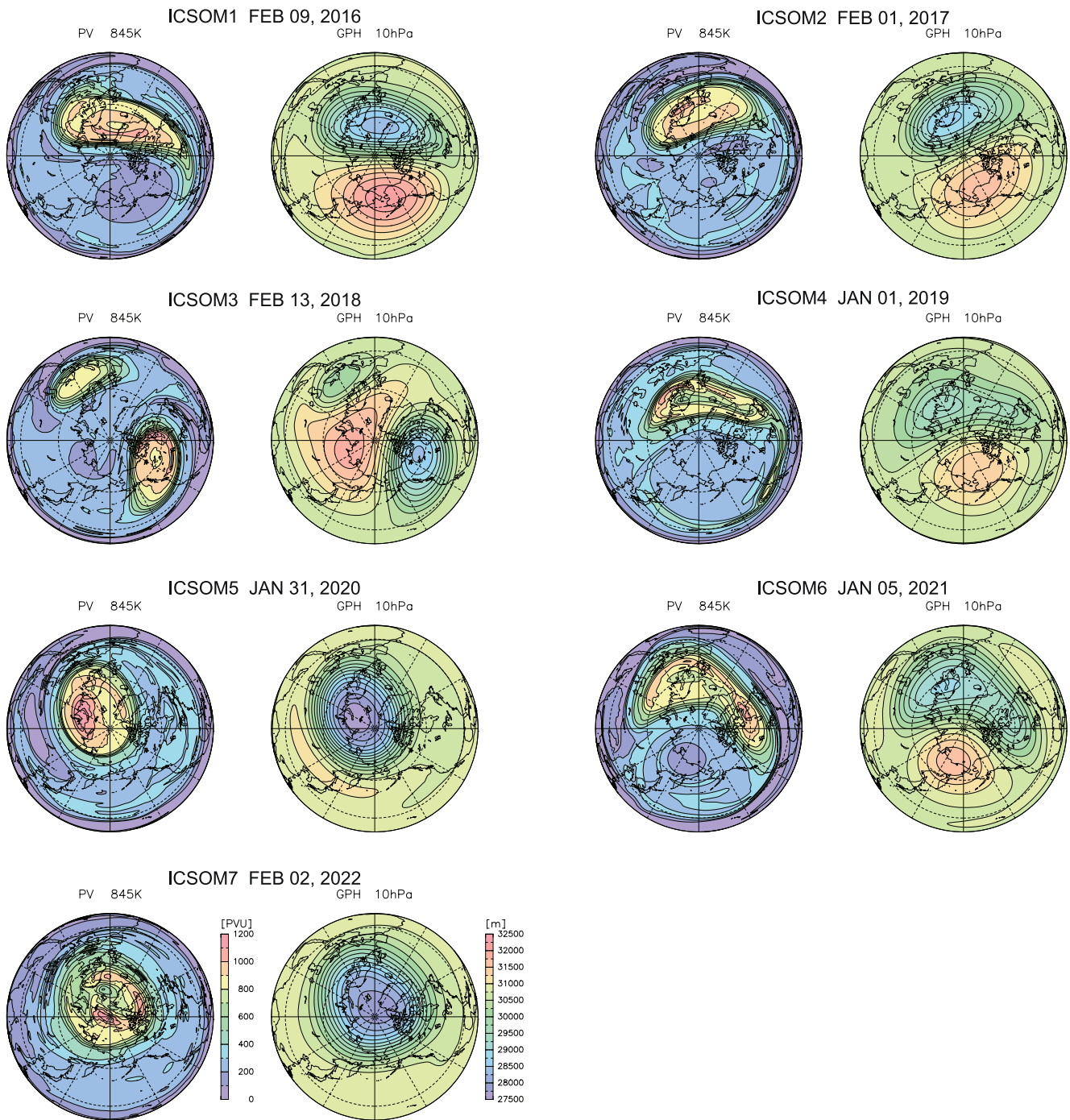
Figure 4. Polar stereo projection maps of potential vorticity at the 845 K isentropic surface and geopotential height at 10 hPa and at the stratospheric sudden warming onset for each campaign. Supplements: movie of Ertel's potential vorticity (PV) at 850 K and geopotential height at 10 hPa for each campaign.

It should be noted that clear and strong stratospheric warm anomaly and mesospheric cold anomaly appear earlier than the SSW onset. Thus, it is appropriate to define the SSW period based on the period of the clear positive and negative anomalies as indicated by the horizontal blue bars. The warm Arctic stratosphere periods for respective campaigns are summarized in Table 3.

For the VI event in ICSOM-5, an opposite behavior with a stratospheric cold anomaly and a mesospheric warm anomaly are observed for $z = 10–40$ km and $z = 50–75$ km, respectively, over the period of 27 January to 2
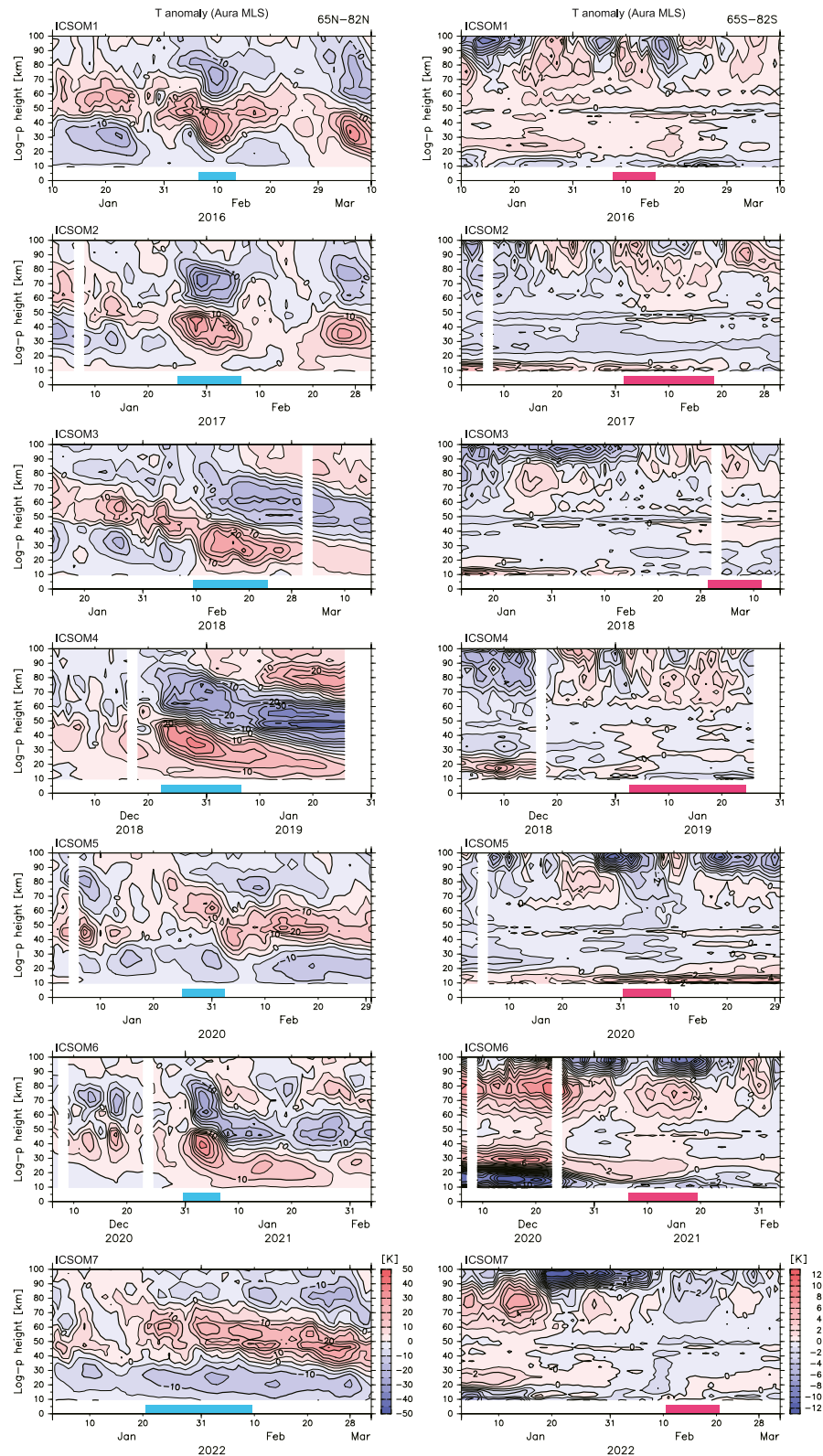
Figure 5. Time-height sections of zonal-mean Microwave Limb Sounder temperature anomaly from the climatology for the Arctic (65°N–82°N) and Antarctic (65°S–82°S) regions for each campaign.

Table 3
Warm (Cold) Arctic Stratosphere Periods and Warm (Cold) Antarctic Mesosphere Periods for ICSOM-1–4 and ICSOM-6 (ICSOM-5)

	Warm Arctic stratosphere period	Warm Antarctic mesosphere period
ICSOM-1	7–13 February 2016	8–15 February 2016
ICSOM-2	26 January–6 February 2017	2–18 February 2017
ICSOM-3	10–23 February 2018	2–11 March 2018
ICSOM-4	22 December 2018–7 January 2019	3–24 January 2019
ICSOM-6	31 December 2020–6 January 2021	7–19 January 2021
	Cold Arctic stratosphere period	Cold Antarctic mesosphere period
ICSOM-5	26 January–2 February 2020	1–9 February 2020
ICSOM-7	21 January–9 February 2022	11–20 February 2022

February 2020. Similarly, for the VI event in ICSOM 7, these anomalies are observed between 21 January and 9 February 2022. In ICSOM-5, another strong and long-lasting anomaly pair appeared around 10 February 2020 at lower altitudes (10–35 km and 40–60 km, not shown for the entire time period in Figure 5), enhancing the polar stratospheric cloud amount and leading to a significant ozone loss in the Arctic (e.g., Lawrence et al., 2020).

As mentioned in Section 1, it has been argued that strong SSWs in the Arctic stratosphere are often followed by a warming in the Antarctic upper mesosphere. The warm anomaly in the upper mesosphere is observed at each event in the Antarctic. However, it seems that the strength of the mesospheric anomaly and the time lag of the appearance after the Arctic stratosphere warming varies with the specific SSW event. The horizontal red bar in the left column of Figure 5 indicates the period of relatively high-temperature anomaly in the Antarctic upper mesosphere observed in each campaign which is probably related to the Arctic stratospheric warming in ICSOM-1, 2, 3, 4, and 6. The Antarctic warm anomaly started around the end of the Arctic stratosphere warm anomaly period for ICSOM-2, 4, and 6, whereas for ICSOM-3, it began 1 week after the end of the Arctic warm anomaly period. The Antarctic warm anomaly for ICSOM-1 is observed almost simultaneously with the Arctic stratosphere warm anomaly. For VI events, opposite signed anomalies, that is, negative anomalies should be expected. The Antarctic upper mesosphere cold anomalies for ICSOM-5 and ICSOM-7, also indicated by red bars, started after almost the end of the Arctic stratosphere cold anomalies. Thus, the correspondence between the behavior in the winter stratosphere versus the summer upper mesosphere is not uniformly consistent in the data shown here. The warm (cold) Antarctic upper mesosphere periods for SSW (VI) events are also summarized in Table 3.

It is worth noting that a strong cold anomaly in the lowermost Southern Hemisphere stratosphere is observed until the end of December 2020 in ICSOM-6. This cold anomaly is related to a large and long-lasting Antarctic ozone hole in 2020 (Stone et al., 2021). It is interesting that a strong warm anomaly is observed around 80 km. This is probably due to vertical coupling with the ozone hole as indicated by Smith et al. (2010). Note also that there are time periods other than those shown by the red bars when positive anomalies can be seen in the Antarctic mesosphere without corresponding SSW events in the Arctic. This result suggests that there are other mechanisms causing warm anomalies in the Antarctic summer mesosphere, which should be carefully distinguished from the response to the Arctic SSWs.

Figure 6 shows a time-height section of the MLS temperature anomaly in the equatorial region (10°S–10°N). When an SSW occurs in the Arctic, the mid- and low-latitude stratosphere becomes cold. Corresponding to the warm anomaly period in the Arctic stratosphere (blue bars), a cold anomaly is observed at the equatorial region at an altitude range of 35–45 km in ICSOM-1, 2, 3, 4, and 6. The low temperature anomaly around $z = 40$ km in ICSOM-3 is short despite the long period of warming in the Arctic stratosphere. In contrast, the warm anomalies expected during the VI events of ICSOM-5 and ICSOM-7 are not significant around $z = 35$–45 km. It has been suggested that a stronger low-temperature anomaly at the equator during the SSW (i.e., a low-temperature anomaly extending to low latitudes) is more likely to be coupled with the summer hemisphere (Yasui et al., 2021). This is consistent with the fact that the warm anomaly in the Antarctic upper mesosphere is prominent in ICSOM-1, 2, 4, and 6 and not clear in ICSOM-3. It should also be noted that the long-lasting temperature anomaly observed
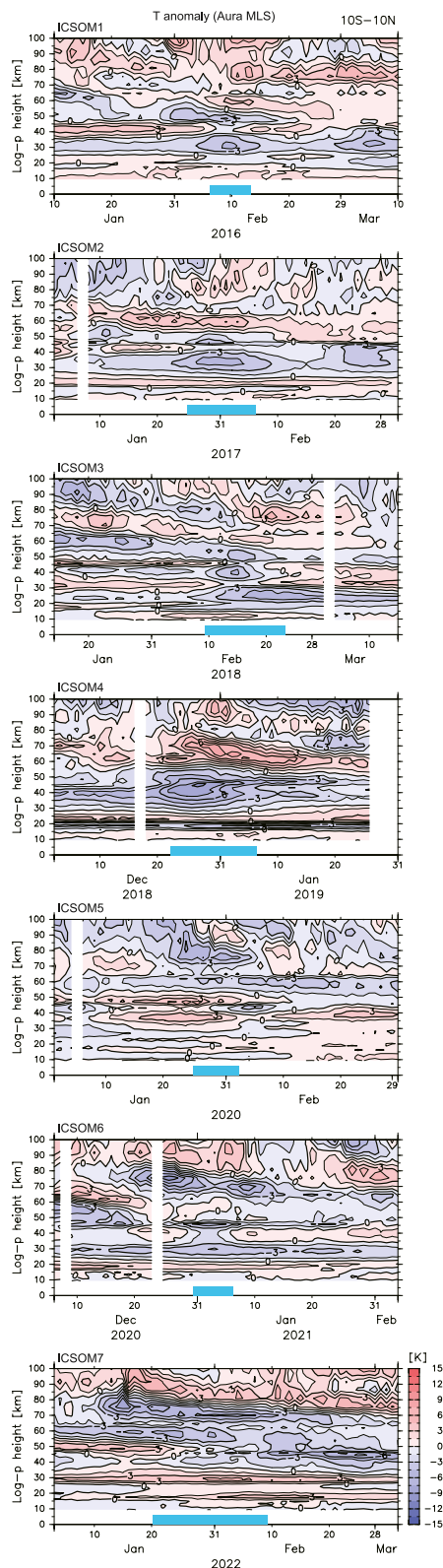
Figure 6. The same as Figure 4 but for the equatorial region (10°S–10°N).

around $z = 25$ km in the equatorial lower stratosphere for ICSOM-3 is thought to be associated with the quasi-biennial oscillation (QBO) (e.g., Freie Universität Berlin, 2023).

4.2. Characteristics of Waves in the Upper Mesosphere in Each ICSOM Campaign Period From Radar Observations

Here we describe the characteristics of GWs and QTDWs in the upper mesosphere observed by the radar network.

4.2.1. GW Kinetic Energy in the Arctic and Antarctic

Figure 7 shows the daily-mean time series of GW kinetic energy divided by density for the altitude range of 85–92 km in the upper mesosphere observed by each radar in the Arctic (left) and Antarctic regions (right). The vertical average for the kinetic energy was calculated by weighting the air density in the form of $\rho(z) = \rho_0 \exp(-z/H)$, where z is the geometric height, ρ_0 is the air density at $z = 0$, and $H = 7$ km. ERWIN data is also included for ICSOM-1. After removing tides from the original time series using the method of Yasui et al. (2016), fluctuation components with wave periods shorter than 1 day are examined as GWs, as was made in Figure 2. Data for ICSOM-7 were not shown because the data set is currently incomplete.

The blue bars in Figure 7 show the time periods with a warm anomaly in the Arctic stratosphere for ICSOM-1 to ICSOM-4, and ICSOM-6 and the time period with a cold anomaly in the Arctic stratosphere for ICSOM-5, as defined in Section 4a (Table 2). It is apparent that the GW kinetic energy in the Arctic mesosphere tends to be small during the warm stratosphere period of 2–5 February 2017 for ICSOM-2, 17–20 February 2018 for ICSOM-3, and 27–31 December 2018 for ICSOM-4 in which major SSWs occurred, although it is not very clear at some sites (e.g., Eureka for ICSOM4). This drop in the GW energy is consistent with the feature responding to the modulation of the mean zonal wind by the SSW as indicated by previous modeling studies (e.g., Tomikawa et al., 2012; Yamashita et al., 2010) and observations (e.g., Thurairajah, Collins, Harvey, Lieberman & Mizutani, 2010; Triplett et al., 2018). The drop is less apparent in the short time series for ICSOM-6. At the end of the warm stratosphere period and thereafter, the GW energy tends to increase in ICSOM-2 and ICSOM-4. While the time variations of the GW kinetic energy observed by radars may not be statistically significant, they will be further investigated in Section 5 through high-resolution GCM simulations fir ICSOM-4. Furthermore, it is worth noting that the radar observation data also provides valuable information for validating models.

The red bars in Figure 7 show the warm anomaly periods in the Antarctic mesosphere. According to the scenario proposed by previous studies such as KB10 and Yasui et al. (2021), the GW energy in the Antarctic upper mesosphere may become weak during this period. This seems to be the case for ICSOM-2 and ICSOM4, and to a lesser extent ICSOM-6 when a major SSW occurred in the Arctic.

For the VI event that occurred in ICSOM-5, clear signals of associated GW modulation are not observed, both in the Arctic and Antarctic.

4.2.2. GW Kinetic Energy in the Northern Middle Latitudes

Figure 8 shows time series of GW kinetic energy divided by density from radar observations at Mohe (54°N, 122°E), Saskatoon (52°N, 107°W), Beijing (40°N, 116°E), and Wuhan (31°N, 115°E) at northern mid-latitudes.
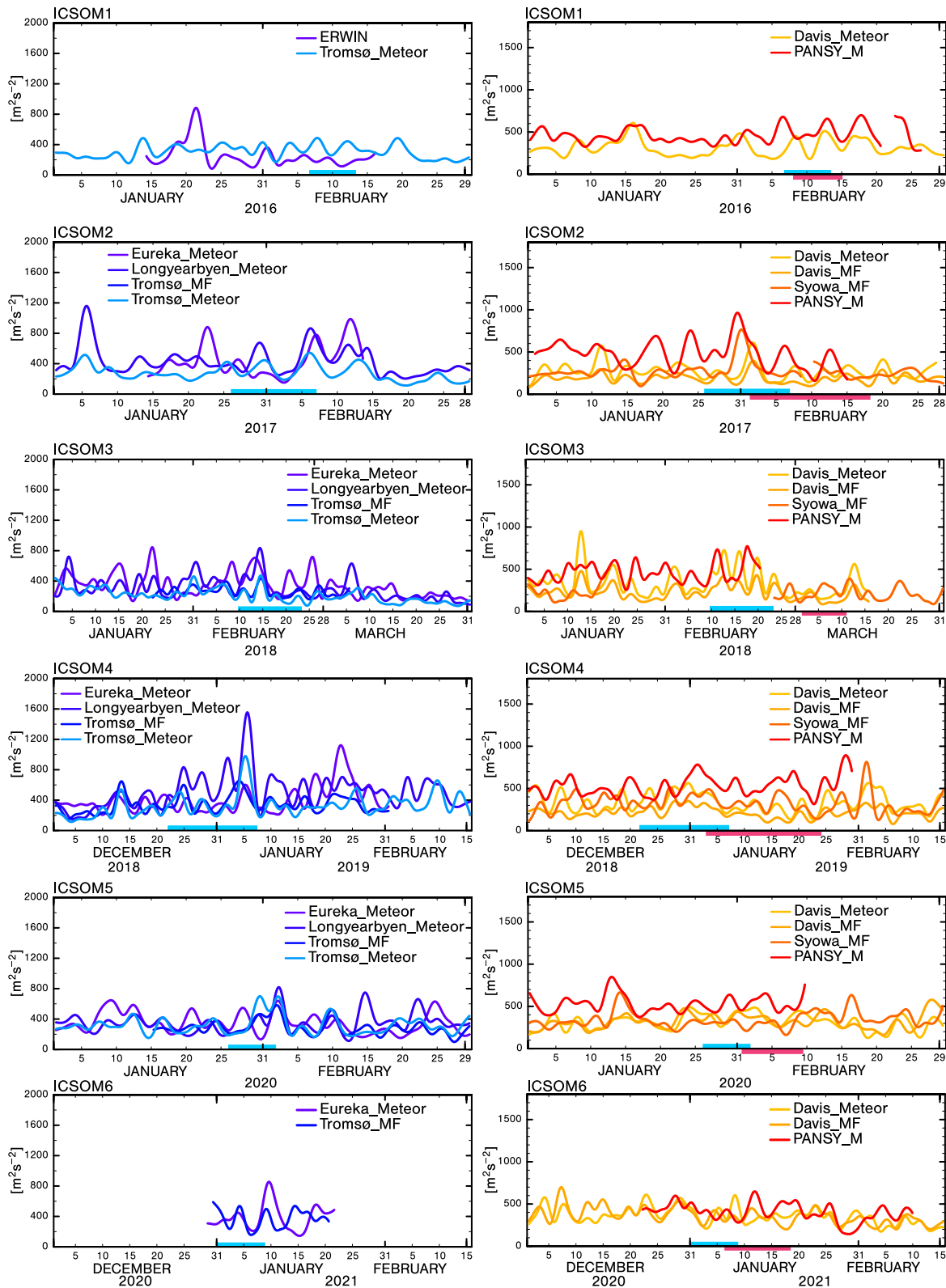
Figure 7. Time-series of gravity wave kinetic energy averaged for $z = 85-92$ km in the upper mesosphere for the Arctic (left) and Antarctic (right) from radar observations for each Interhemispheric Coupling Study by Observations and Modelling campaign. The blue bars indicate the warm period in the Arctic stratosphere and the red bars indicate the warm period in the Antarctic upper mesosphere.
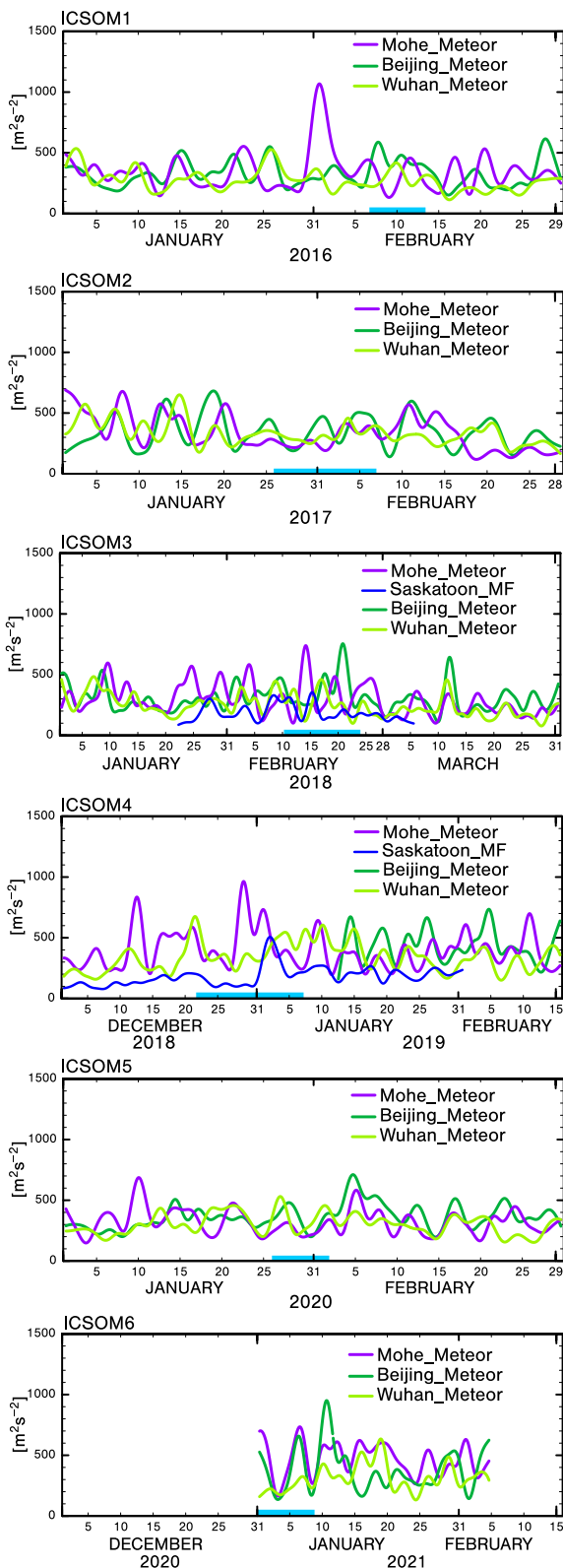
Figure 8. The same as Figure 7 but for the northern middle latitudes.

The blue bars indicate the Arctic stratosphere warm anomaly period. During this period, GW kinetic energy is expected to be small, even at mid-latitudes, if the mean zonal wind modulation extends latitudinally in association with a strong SSW. Such a decrease can be seen at the beginning of the warm anomaly period in ICSOM-2 and ICSOM-4 in most stations. As shown in detail later for ICSOM-4, the negative (westward) anomaly of zonal wind associated with the SSW extended to about 20°N in the height region of 30–85 km in the stratosphere and mesosphere. This mean wind anomaly feature is consistent with the observed GW kinetic energy reduction.

4.2.3. Quasi-Two Day Wave Kinetic Energy in the Antarctic

We also examined time variations of QTDWs observed by radars. It is known that QTDWs increase in amplitude after the summer solstice (e.g., Ern et al., 2013; Vincent, 2015). The QTDWs are understood to be generated by dynamical instabilities, namely the BT/BC instability of the summer easterly jet (e.g., Plumb, 1983), and the BT/BC instability is thought to be caused by forcing of primary GWs originating from the troposphere (e.g., Ern et al., 2013; Sato et al., 2018) and also by inertial instability (Lieberman et al., 2021). Previous studies indicated that stronger QTDWs in the mesosphere of the Southern Hemisphere can cause stronger westward forcing which weakens the summer meridional circulation resulting in the warm Antarctic upper mesosphere (France et al., 2018; Siskind & McCormack, 2014; Yasui et al., 2021).

It has been suggested that the QTDW enhancement in the summer mesosphere is related to planetary-wave activity in the winter hemisphere. France et al. (2018) showed that the strong planetary-scale wave breaking in the winter stratosphere in the Southern Hemisphere is accompanied by an enhanced easterly jet in the summer mesosphere in the Northern Hemisphere, which strengthens the QTDW generation. A statistical study focusing on stratospheric warming in the Northern Hemisphere was made by Yasui et al. (2021). They pointed out the importance of the cold anomaly in the equatorial region accompanied by the warm anomaly in the high latitude region in winter for IHC. The equatorial cold anomaly enhances the easterly jet in the Southern Hemisphere summer mesosphere, which increases the occurrence frequency of BT/BC instability radiating QTDWs in the mesosphere.

The time series of QTDW kinetic energy divided by density observed by radars in the Antarctic are shown in Figure 9. The QTDW variances have a broad maximum around January 20 in ICSOM-2, ICSOM-3, ICSOM-4, and ICSOM-5, which is consistent with the daily QTDW climatology shown by a statistical analysis by Ern et al. (2013). The QTDW variance at this maximum is particularly large in ICSOM-4, where a major SSW occurred in early January. This may correspond to the significant warm anomaly around January 20 in the Antarctic upper mesosphere (Figure 5), however, it is difficult to distinguish it from the seasonal variation of QTDW climatology.

5. Dynamical Characteristics of Waves and Mean Field During ICSOM-4

5.1. Time-Height Section of Zonal-Mean Zonal Wind

The left column of Figure 10 shows time-height sections of zonal-mean zonal wind for the northern high-latitude region of 50°N–70°N, the equatorial region of 10°N–10°S and the southern high-latitude region of 50°S–70°S for ICSOM-4 from the JAGUAR-DAS reanalysis data set. The right column of
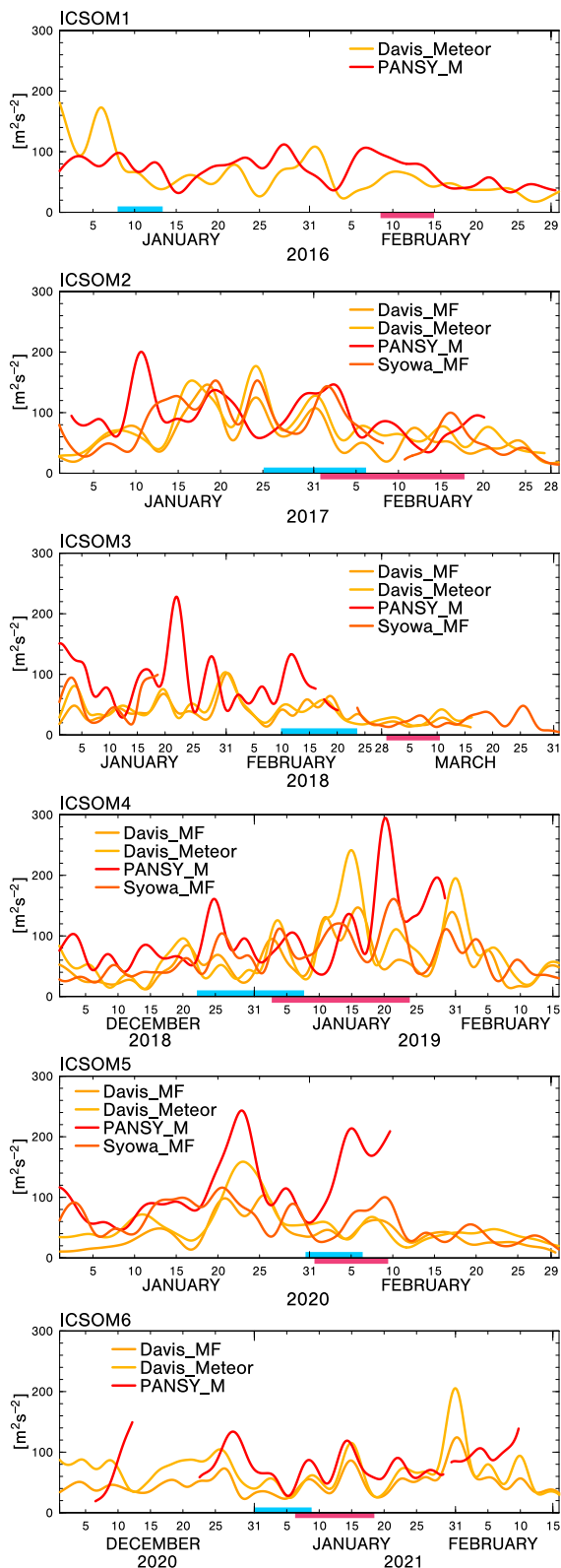
Figure 9. The same as Figure 7 but for quasi-two-day waves in the Antarctic upper mesosphere.

Figure 10 shows the anomaly for each region, where the anomalies are calculated as the departure from the climatology, which is an average over 15 years from January 2005 to December 2019. To see the sub-seasonal variation more clearly, a low pass filter with a cutoff period of 4 days was applied.

In the northern high latitude region, easterly winds appear in the time period of 25 December 2018 to 26 January 2019 gradually propagating downward from $z = \sim 50$ km to $z = \sim 25$ km in association with the time evolution of the major SSW with its onset on 1 January 2019. The zonal wind near $z = 80$ km was also weakly easterly in 23–29 December 2018 and returned to westerly after that. The westerly wind was once again weakened around 8 January 2019 but became stronger again after that. Then, a strong westerly reaching 100 m s^{-1} was formed around $z = 60$ km on 22 January 2019. This drastic variation of the zonal winds associated with the SSW event can be more clearly seen in the anomaly. The variation is dominant in almost the whole middle atmosphere from $z = 20$–90 km.

It is worth noting here that a critical layer for orographic GWs (i.e., the mean zonal wind is zero) is observed from 25 December 2018 at $z = \sim 40$ km to 25 January 2019 at $z = \sim 25$ km. This critical layer is also continuously observed at higher latitudes (not shown). The long-lasting thin wavy structure observed in model-simulated GW components at Eureka at $z = \sim 30$ km from 27 December 2018 to 4 January 2019 in Figure 3 is consistent with an orographic GW's behavior below a critical layer.

In the equatorial region of 10°S–10°N, strong easterly winds are observed around $z = \sim 50$ km during the warm Arctic stratosphere period from 23 December 2018 to 6 January 2019. The maximum magnitude of the easterly winds is greater than 100 m s^{-1} around 7 January 2019. This is considered to be a feature commonly observed as a part of the equatorial semi-annual oscillation in the upper stratosphere. However, it is seen from the anomaly shown on the right that the easterly wind is stronger than usual. A westerly wind anomaly is also observed above the easterly wind anomaly. This feature is related to the checkerboard pattern of temperature anomalies associated with the SSW event shown in the next subsection. Note that the continuous strong westward wind anomaly observed below $z = \sim 25$ km is due to the quasi-biennial oscillation in the stratosphere.

In the southern high-latitude region of 50°S–70°S, strong easterly winds are observed in the upper mesosphere. The maximum is located at $z = 75$ km on 2 December 2018 and descends gradually to reach $z = 70$ km on 31 January 2019. A weak wind region with magnitudes smaller than 10 m s^{-1} in the uppermost mesosphere gradually descends after 25 December 2018 in the height region of $z = 90$–100 km. This feature is mainly due to seasonal variation. During most of the warm period for the Antarctic upper mesosphere from 3–24 January 2019, wind anomalies are negative in the height region of $z = 65$–95 km and positive below that, although their magnitude is weak, up to 2.5 m s^{-1}.

5.2. Latitude-Height Section of Zonal-Mean Temperature, Zonal Wind, EP Fluxes, and Residual-Mean Flow

Using the JAGUAR-DAS data set, the zonal-mean fields and their anomalies from the climatology are examined in the latitude-height section for ICSOM-4. The left column of Figure 11 shows zonal-mean temperatures for four time periods of 11–20 December 2018, 21–30 December 2018, 31 December 2018 to 9 January 2019, and 10–19 January 2019. The Arctic
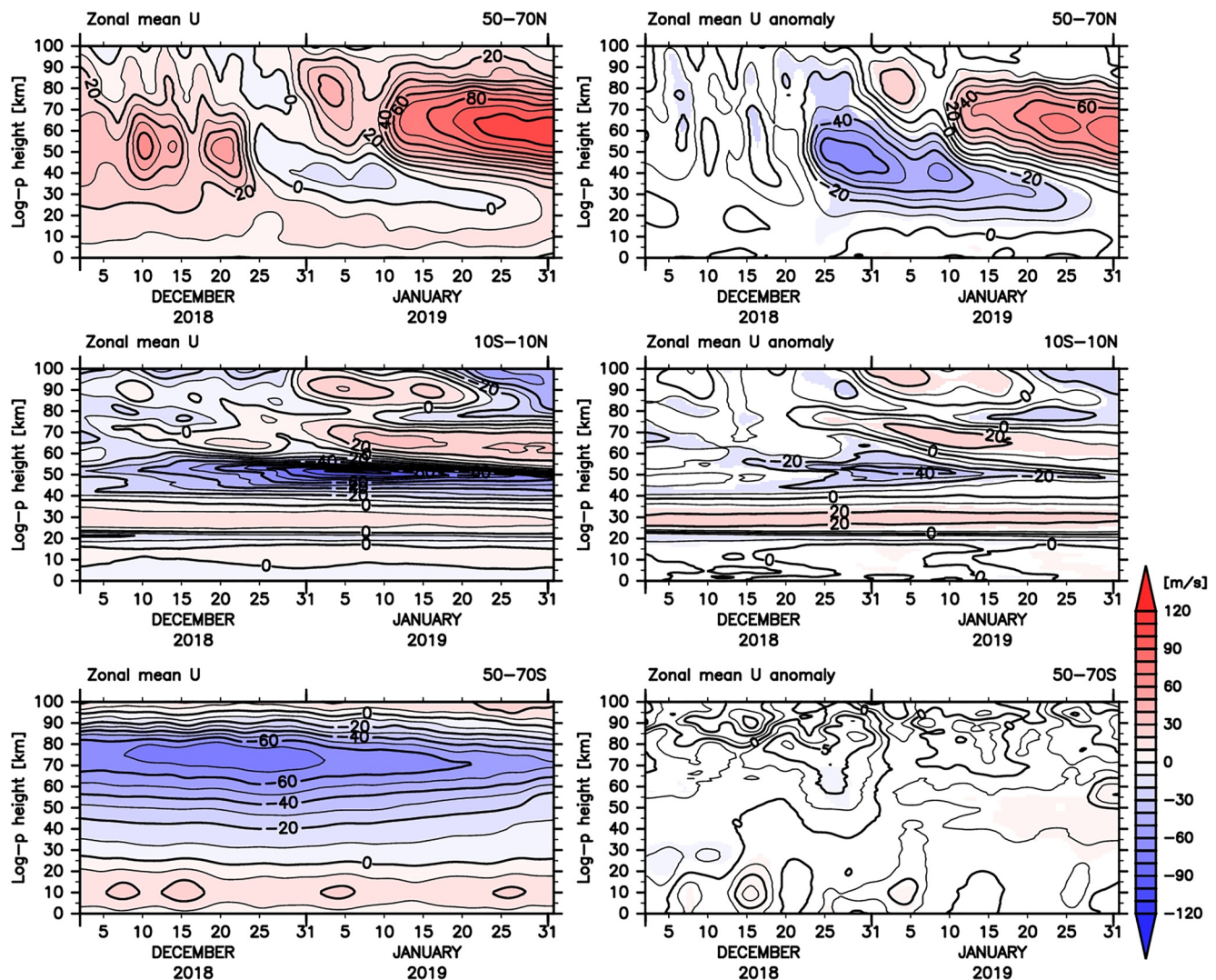
Figure 10. Time-height section of zonal-mean zonal winds and their anomaly from climatology for 50–70°N, 10°S–10°N, and 50–70°S in ICSOM-4 from JAGUAR-DAS. Contour intervals are 10 m s^{-1} except for the zonal-mean zonal wind anomaly for 50–70°S in which contour intervals are 2.5 m s^{-1}. Color shaded are the regions with anomalies greater than a standard deviation.

stratopause is located at a normal height at $z = \sim 55$ km in the first period of 11–20 December 2018 and was gradually lowered between 21 and 30 December to reach the height of $z = \sim 35$ km due to the SSW. The stratopause was reformed at a high altitude of $z = \sim 85$ km in 10–19 January 2019. A detailed analysis on the dynamics of this time evolution of the stratopause was made by Okui et al. (2021) based on the simulation of a GW-permitting GCM.

The right column of Figure 11 shows the zonal-mean temperature anomaly from the climatology for ICSOM-4 in the same four time periods. Color shaded are the regions with anomalies greater than a standard deviation. Weak warm anomalies are already observed in the northern high latitude region in the first time period of 11–20 December 2018. The warm anomalies are strengthened and extend to middle latitudes centered at $z = \sim 36$ km in 21–30 December 2018. Significant cold anomalies are observed above the warm anomalies and also in the equatorial upper stratosphere extending to 20°S. The equatorial cold anomaly in the upper stratosphere is similar to the favorable condition for IHC indicated by Yasui et al. (2021). These anomalies, along with a warm anomaly in the equatorial region observed above the cold anomaly, form a large-scale checkerboard pattern in the latitude region from 20°S to the North Pole.
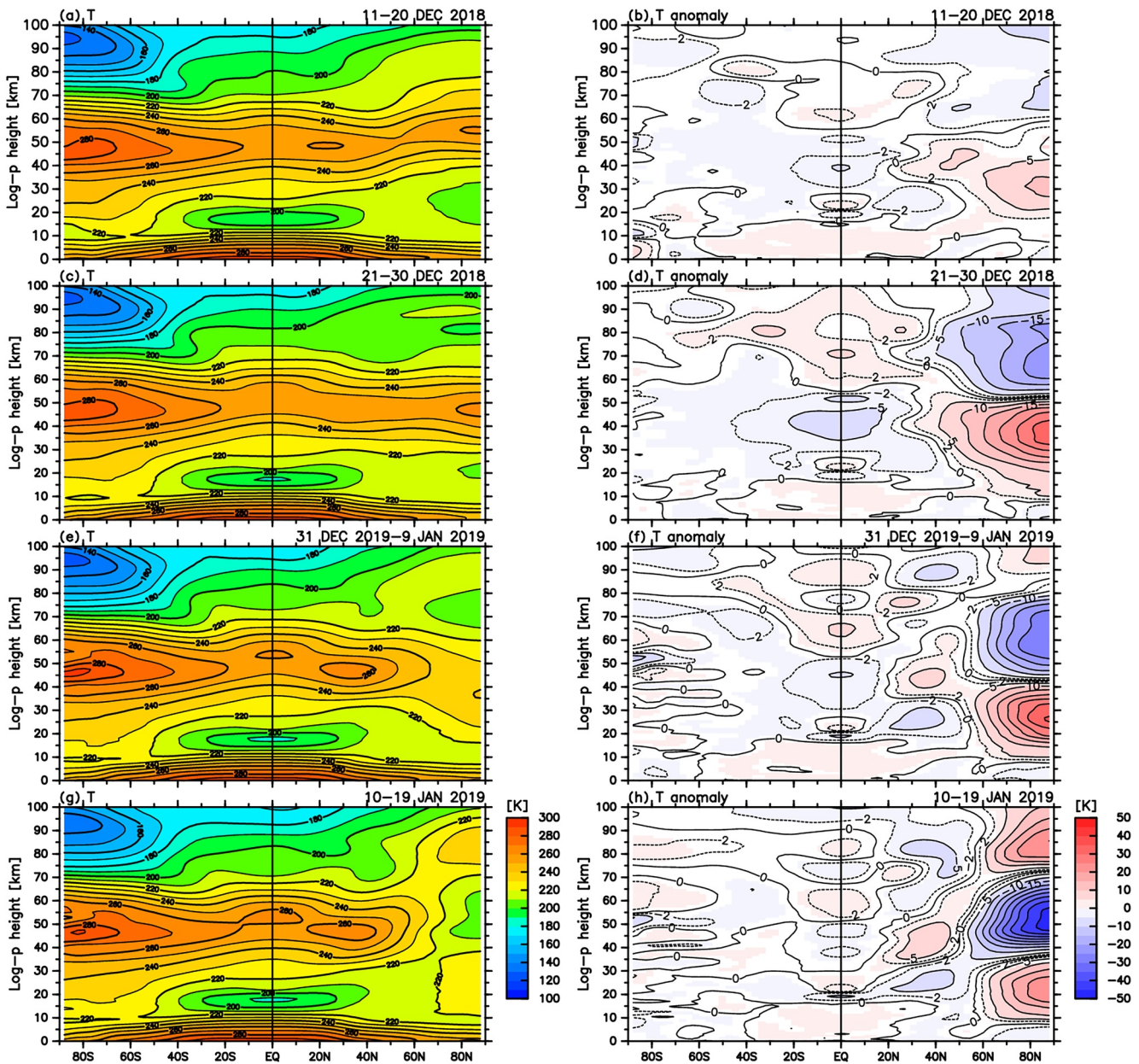
Figure 11. A series of zonal-mean temperature (left) and its anomaly from the climatology (right) in the meridional cross section from JAGUAR-DAS at (a) (b) 11–20 December 2018, (c) (d) 21–30 December 2018, (e) (f) 31 December 2018–9 January 2019, and (g) (h) 10–19 January 2019 for ICSOM-4. Contour intervals are 10 K for the zonal-mean temperature and 2.5 K for the anomaly. Color shaded are the regions with anomalies greater than a standard deviation.

During 31 December 2018 to 9 January 2019, the checkerboard pattern is more evident but observed in the narrower latitude region of 20°N–90°N in $z = 10$–60 km than in the previous time period. In addition, warm anomalies are recognized at southern latitudes higher than 60°S. From 10–19 January 2019, the warm and cold anomalies in the Northern Hemisphere descend by $\sim$5 km and another warm anomaly region appears around $z = 85$ km corresponding to the elevated stratopause observed in the zonal-mean temperature in Figure 11g. It is also worth noting that warm anomalies greater than 2 K are observed in the southern upper mesosphere around $z = 80$ km in 40°S–90°S. This feature is consistent with the IHC associated with the Arctic SSW indicated by previous studies (e.g., Karlsson, McLandress, et al., 2009; Naren Athreyas et al., 2022; Yasui et al., 2021).

The Eliassen-Palm (EP) fluxes and their divergence (i.e., wave forcing) in the primitive equation system (Andrews et al., 1987) are shown in the left column of Figure 12 for the same four time periods shown in Figure 11, together
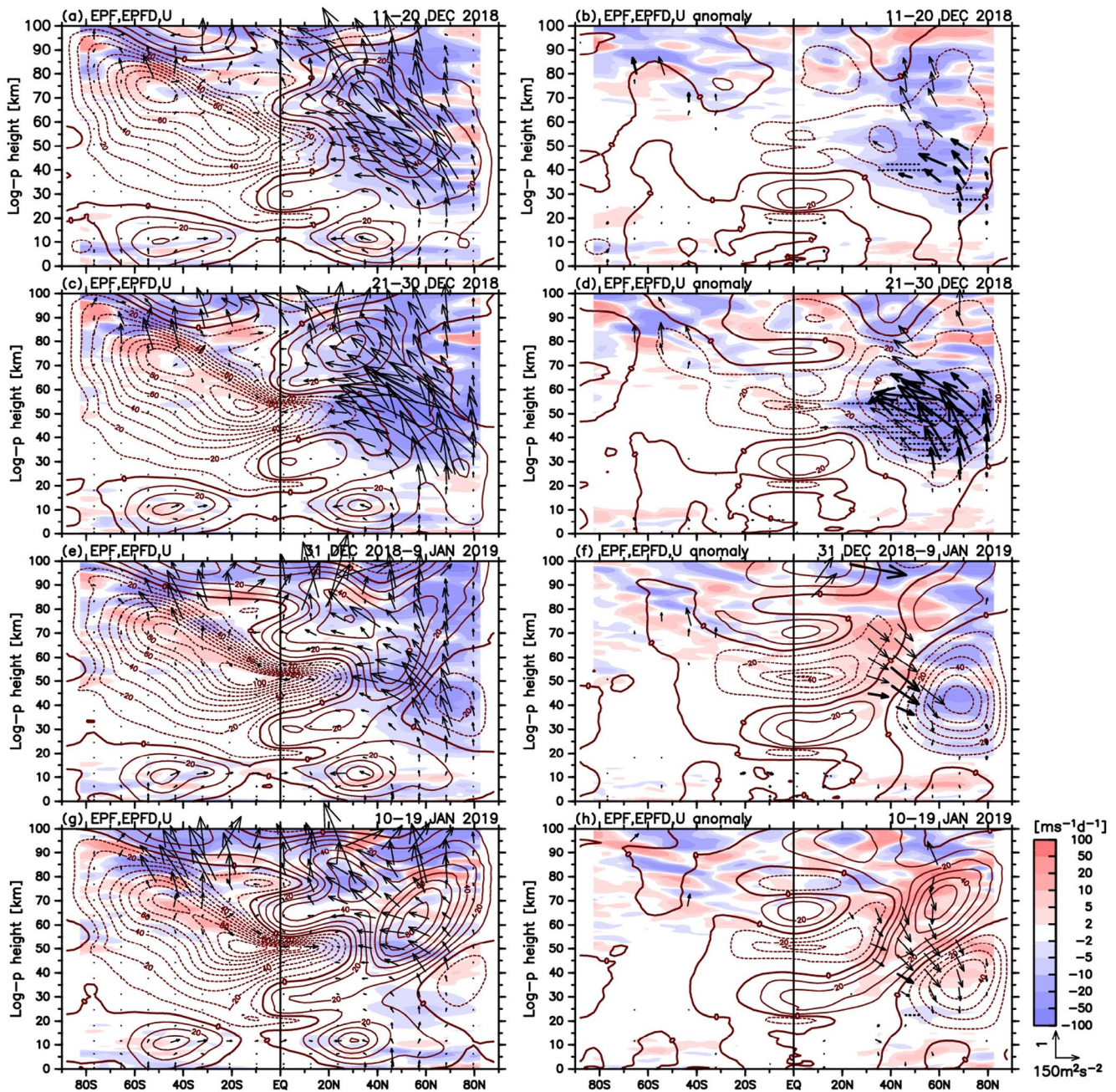
Figure 12. The same as Figure 11 but for E-P flux (black arrows), E-P flux divergence (color contours), and zonal-mean zonal wind $\bar{u}$ (dark brown line contours). Contour intervals are 10 m s^{-1} for both $\bar{u}$ and $\bar{u}$ anomalies. Note the unit lengths of E-P flux vectors and color contours for E-P flux divergence are the same for all panels. Thick and thin arrows indicate EP flux anomalies with magnitudes exceeding one and a half standard deviations, respectively. The dotted area highlights regions with EP-flux divergence anomalies greater than one standard deviation.

with the zonal-mean zonal wind. It is clear that strong resolved waves which are mainly planetary waves propagate upward from the troposphere and give significant westward forcing in a wide height region above $z = 30$ km in middle and high latitudes of the Northern Hemisphere. This occurs in the first two time periods leading up to the major SSW (with its onset on 1 January 2019), and in the third time period of 31 December 2018 to 9 January 2019. The planetary waves propagate even in the easterly wind region observed during the third time period, which contradicts the theory of Charney and Drazin (1961) at a glance. According to Okui et al. (2021), however, these planetary waves could propagate through a limited longitudinal region where the zonal wind is westerly.

The anomaly fields are displayed in the right column of Figure 12, where thick and thin arrows indicate EP flux anomalies with magnitudes exceeding one and a half standard deviations, respectively. The dotted area highlights regions with EP-flux divergence anomalies greater than one standard deviation. The strong upward and equatorward propagation of planetary waves is clear in the anomaly fields particularly in the first and second time periods in the Northern Hemisphere. Strong negative EP-flux divergence (i.e., westward forcing) anomalies are also observed in the first and second time periods, as is consistent with the characteristics of a strong SSW. It is worth noting that the EP-flux vectors are plotted with the same scale both for total fields and anomaly fields, indicating that anomalies are quite strong and of the same order as the climatology. In contrast, in the third and fourth time periods, downward and poleward EP-flux are dominant in the middle and high latitudes in the upper stratosphere and lower mesosphere of the Northern Hemisphere, showing weaker planetary wave propagation than the climatology.

Negative EP-flux divergence, as well as, strong upward and poleward EP flux are observed in the southern middle latitudes of the upper mesosphere over all four time periods, suggesting that resolved waves also contribute to the residual circulation. Positive EP-flux divergence is observed near the upper region of the easterly jet in the Southern Hemisphere, indicating in-situ generation of resolved waves in the mesosphere. The EP flux and its divergence appear to be enhanced, as suggested by the anomaly fields in the first to third time periods, although they are not significant. These EP-flux divergence anomalies may be related to the warm anomalies are observed in southern middle and high latitudes around $z = 85$ km in the second to fourth time periods, as seen in Figure 11. It should be noted that these features are consistent with the suggestion by Siskind and McCormack (2014) and Yasui et al. (2021), which proposes that in-situ generated large-scale waves, primarily due to the QTDWs, play an important role in the IHC.

Figure 13 shows the meridional cross section of the meridional component of the residual mean flow $\overline{v}^*$ on the left and its anomaly from the climatology on the right for the same four time periods shown in Figure 11. Basically speaking, in the upper mesosphere of both hemispheres and in the upper stratosphere around $z = 50$ km between ~5°S and 55°N, the residual mean flow $\overline{v}^*$ is primarily strongly positive (i.e., northward) for all four time periods, which is consistent with the climatological view (e.g., Plumb, 2002).

The northward $\overline{v}^*$ in the upper stratosphere is particularly strong in the second and third time periods as is recognized in the $\overline{v}^*$ anomaly, which is likely related to the occurrence of the SSW. On the other hand, the negative EP flux divergence anomaly in the upper stratosphere is strong in the first and second time periods (Figure 12). The time difference between the northward $\overline{v}^*$ anomaly and the negative EP flux divergence anomaly in the upper stratosphere suggests that the former is the transient response to the latter. A strong equatorward flow anomaly is observed near $z = 75$ km in the upper mesosphere from ~5°S to northern high latitudes, which is also consistent with the transient response to the negative EP flux divergence anomaly in the upper stratosphere (e.g., Smith et al., 2020). However, it seems that the positive and negative $\overline{v}^*$ anomalies observed in the upper stratosphere and in the upper mesosphere, respectively, do not extend deeply enough into the Southern Hemisphere to produce the IHC that is the focus of the present study.

In the Southern Hemisphere, a strong positive $\overline{v}^*$ is observed from 30°S, $z = 85$ km to 75°S $z = 100$ km for the first three time periods and at slightly lower altitudes for the last time period. Positive and negative $\overline{v}^*$ anomalies are observed slightly below and above the strongly positive $\overline{v}^*$ region, respectively. The negative $\overline{v}^*$ anomaly is particularly evident in the last two time periods, which is consistent with the positive temperature anomaly observed in Figures 11f and 11h. This strong negative $\overline{v}^*$ anomaly in the last two time periods may be the transient response of the residual mean flow to the negative EP flux divergence anomaly in the southern middle latitudes of the upper mesosphere that are observed in the second and third time periods (Figures 12d and 12f).

5.3. GWs in the Upper Mesosphere in ICSOM-4 Simulated by a GW-Permitting GCM and Observed by SABER

Time variation of GW energy in the upper mesosphere responding to the Arctic SSW can be examined using the GW-permitting GCM (JAGUAR) simulation outputs. As the GWs have significant seasonal variations (e.g., Sato et al., 2009; Tsuda et al., 1990), the IHC signals should be analyzed for the anomaly from a climatology that is calculated using simulations covering several decades. However, simulations by the GW-permitting GCM over decades are not available due to limitations of current computer resources. The zonal-mean GW kinetic energy
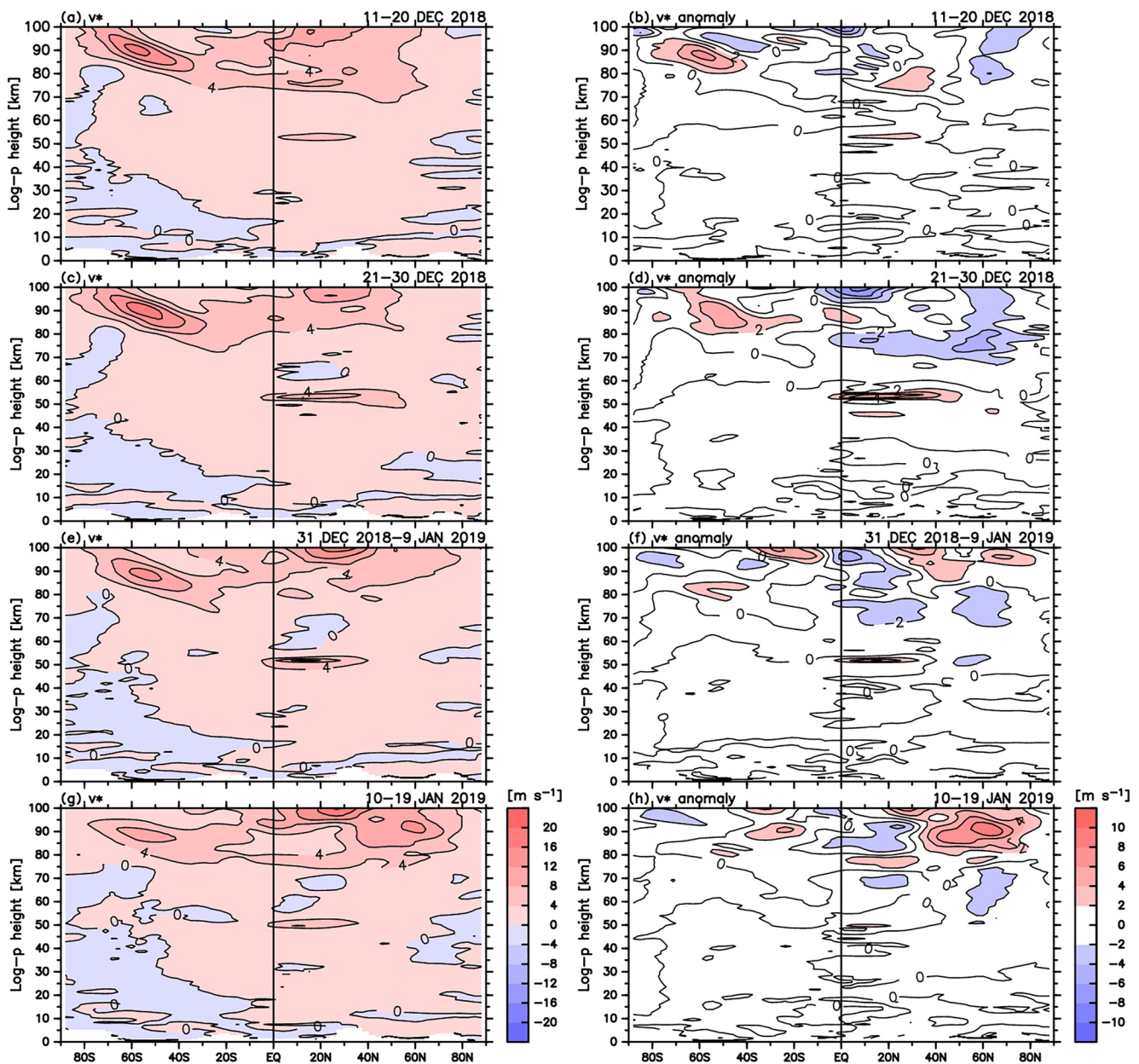
Figure 13. The same as Figure 11 but for the meridional component $\overline{v}^*$ of residual-mean flow. Contour intervals are 4 m s^{-1} for $\overline{v}^*$ (left) and 2 m s^{-1} for its anomaly (right).

divided by density in the upper mesosphere (z = 85–92 km) from the GW-permitting GCM for ICSOM-4 is shown in the time-latitude section in Figure 14a. Here, fluctuations with total horizontal wavenumbers of 21–639 are designated as GWs. The same vertical average with a weight of the air density is applied for Figure 14 as for Figures 7–9. As the simulations were performed for each 4-day time period, a 4-day running mean was applied to the model-simulated GW field to eliminate slight trends that depend on the time after each simulation start time. This means that the displayed time variation is effectively lowpass filtered with a cutoff period of ~8 days. Vertical lines in Figure 14a shows the boundaries of the model data from each simulation.

The GW kinetic energy divided by density is minimized in the time period around 27 December 2018 in the latitude region of 20°S–85°N, maximized around 5 January 2019 and minimized around 10 January 2019 in 50°N–80°N. The previous minimum around 27 December 2018 is roughly consistent with the features of GW
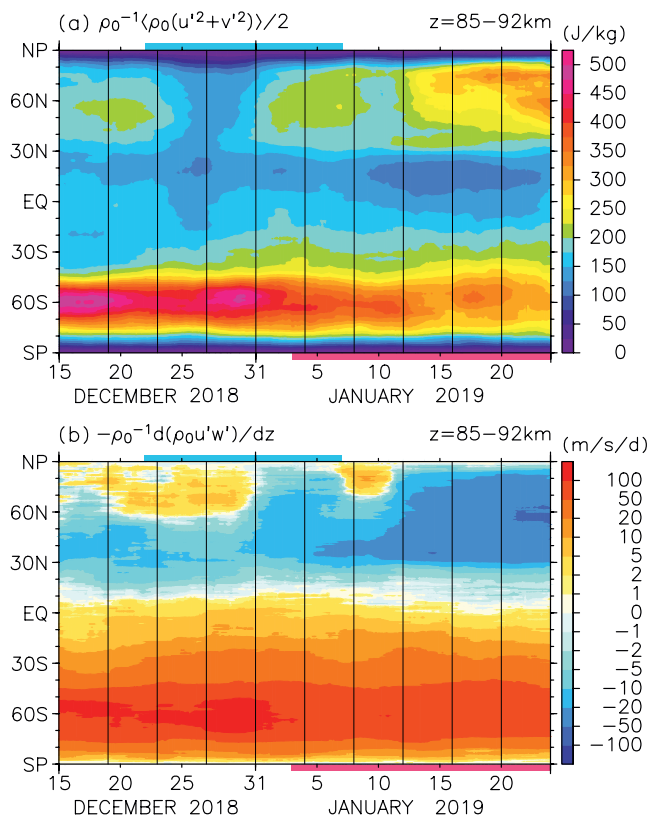
Figure 14. Time-latitude section of gravity wave kinetic energy and zonal momentum flux divergence for z = 85–92 km simulated by gravity-wave permitting general circulation model (JAGUAR) for ICSOM-4. The blue bars indicate the warm period in the Arctic stratosphere and the red bars indicate the warm period in the Antarctic upper mesosphere.
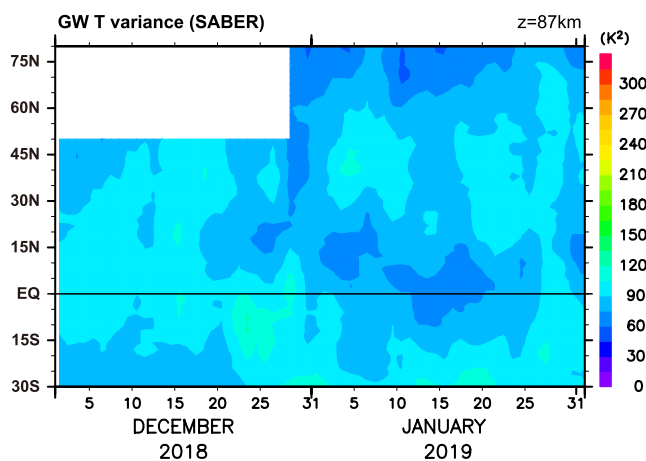
Figure 15. Time-latitude section of gravity wave temperature variances at z = 87 km from Sounding of the Atmosphere using Broadband Emission Radiometry (SABER) observations for ICSOM-4.

kinetic energy observed by the radars in the Arctic shown in Figure 7 and in the northern middle latitudes in Figure 8. The maximum around 5 January 2019 and minimum around 10 January 2019 are consistent with the radar observations in the Arctic (Figure 7). During the weak GW kinetic energy periods around 27 December 2018 and 10 January 2019, the zonal-mean zonal winds are weak westerly or rather easterly in most middle atmosphere northern high latitudes (Figure 10a). This is consistent with the expected response of GWs in the strong SSW (e.g., Thurairajah et al., 2014; Tomikawa et al., 2012; Yamashita et al., 2010) and an analysis of mesospheric airglow images (Tsuchiya et al., 2018). In the Southern Hemisphere, however, significant GW signals responding to the SSW are not apparent (Figure 14a), as is consistent with radar observations (Figure 7). A slight decrease in the GW kinetic energy near 15 January around 60°S may be significant. A gradual decrease in the GW kinetic energy during 1–18 January 2019 may instead be a part of the seasonal variation. This unclear variation suggests that the response of GWs in the Southern Hemisphere to the SSW in the Northern Hemisphere is weak compared with the seasonal variation.

Figure 14b shows the GW forcing estimated as the vertical convergence of the vertical flux of zonal momentum associated with the GWs in the time-latitude section for z = 85–92 km. In the normal condition of the Northern (Southern) Hemisphere, the GW forcing is expected to be westward (eastward) (e.g., Alexander et al., 2010) as seen after 12 January 2019. However, positive GW forcing at northern high latitudes is observed from 19–30 December 2018 and 7–11 January 2019. These time periods roughly correspond to those with weak westerly or rather easterly zonal winds in most of the middle atmosphere below the upper mesosphere (Figure 10a). Note that these time periods include 26–28 December 2018 when the GW kinetic energy is minimized. This feature is likely related to the lack of orographic GWs due to critical level filtering far below, which would normally cause westward forcing in the upper mesosphere, and because non-orographic GWs having eastward phase velocity relative to the mean wind easily survive and break in the upper mesosphere (e.g., Limpasuvan et al., 2016; Thurairajah, Collins, Harvey, Lieberman, Gerding, et al., 2010). During this time period, the westward GW forcing is weakened in the Northern Hemisphere middle latitudes where GW kinetic energy is similarly minimized. However, the modulation of GW forcing is not very clear in the equatorial region and in the Southern Hemisphere, for example, the tropical region around 27 December 2018 and the latitude region around 60°S around 15 January 2019 where a GW kinetic energy minimum was observed.

Figure 15 shows the time-latitude section of the GW temperature (T) variances at z = 87 km observed by SABER. The GW components are extracted following Ern et al. (2018) as described in Section 2b. Similar lowpass-filtered variations to Figure 14 are shown. Due to its yaw cycle, SABER observes up to 50°N before 28 December 2018 and 80°N later. In addition, due to enhanced noise in the summertime measurements of the mesopause region, only latitudes northward of 30°S are shown.

The GW T variances are minimized around 29 December 2018 at latitudes higher than 20°N, and maximized around 7 January 2019 and minimized around 10 January 2019 at latitudes higher than 55°N. These satellite measurements of maxima and minima in wave activity are roughly consistent with the radar observations and the GCM-simulated GW kinetic energy at these times and locations. There are some differences in the time series of the GW variances at low latitudes between SABER observations and the GCM simu-

lation. This difference may be explained by the local solar time variations of the SABER observation due to orbit precession as well as due to the satellite yaw maneuvers.

6. Summary and Future Plans

To elucidate the mechanism of the coupling between the Northern and Southern Hemispheres through the mesosphere, that was discovered shortly before 2010, it is necessary to investigate the global variations of GWs and other waves such as QTDWs in the real atmosphere that are involved in this coupling. However, until now, there have been few observational and modeling resources available and capable of investigating the mechanism of this coupling. This is because the mechanism is expected to include the roles of in-situ generation and dissipation of these waves in the middle atmosphere and the lateral propagation of GWs. Both of these physical processes on GWs are usually ignored in the parameterization in climate models. The objective of this study is to elucidate the dynamical mechanism of the IHC through a combination of simultaneous observations by a sparse but globally distributed network of 31 radars that monitor wind fluctuations in the upper mesosphere in a framework of the international collaboration. The analysis capability is enhanced by the development of a new data assimilation system, JAGUAR-DAS, for the entire middle atmosphere (i.e., stratosphere, mesosphere, and lower thermosphere) using satellite temperature and radiance data to generate long-term global reanalysis data, and simulations by a GW-permitting GCM, a high-resolution version of JAGUAR, that is initialized with the reanalysis data. This initial study shows consistent variations in the circulation and GW activity during SSW and IV events between observations from a network of ground-based radars and satellites and high-resolution model simulations.

Seven international campaigns of joint radar observations during Arctic winter SSWs and polar VI events were successfully performed. The participating radars were atmospheric (MST) radars, meteor radars, and MF radars which provide time series of wind fluctuations to capture GWs in the mesosphere. Lidars, which measure temperature and partly wind fluctuations, optical imagers to observe airglows, and IS radars to observe the time variation of the ionosphere have also participated, although results are not shown in the present paper. Our initial analysis of these radar observation data, drawing on observations from 12 of these radars, suggests a strong case-dependence of the GW variability in response to each SSW.

JAGUAR-DAS uses a 4D local ensemble transform Kalman filter, which allows for long-term reanalysis at relatively low computational cost. The global response (i.e., anomaly) to the SSW in the Northern Hemisphere during ICSOM-4, when a major SSW occurred, was examined using the JAGUAR-DAS reanalysis data. The climatology used to calculate the anomaly was obtained using reanalysis data over 15 years from January 2005 to December 2019. It was confirmed that the temperature anomaly in the upper mesosphere of the Southern Hemisphere was roughly consistent with features indicated by previous modeling studies. The anomaly also shows an increase in the EP flux and its divergence (i.e., wave forcing) associated with model-resolved waves, which is thought to be due to Rossby waves and Rossby-gravity waves, in the data assimilation system. These results suggest that not only GWs but also large-scale waves are important for the mechanism of the IHC.

An analysis for ICSOM-4 was also carried out for the simulation data by the GW-permitting JAGUAR, which extends from the troposphere to the lower thermosphere, using the reanalysis data for its initial conditions. It was shown that the modulation (i.e., a tentative energy decrease) of GWs in the upper mesosphere associated with the SSW is clear in the region from the Arctic to the Southern Hemisphere subtropics, and is consistent with several radar observations. In contrast, the GW response to the SSW in the middle and high latitudes of the Southern Hemisphere are too weak to be detected in the seasonal variations of GWs. It was confirmed that these features are roughly consistent with satellite observations by SABER. These results indicate that the high-resolution JAGUAR has ability to simulate realistic GWs and can be a powerful research tool to examine the variability of the whole middle atmosphere in which waves with a wide range of spatial and temporal scales are embedded.

In the future, more comprehensive investigations should be conducted to quantify the contribution to the IHC not only by primary GWs from the troposphere but also by tidal waves, secondary GWs, and Rossby/Rossby-gravity waves that are generated in the middle atmosphere, by the 3D propagation of these waves, and by the inertial instabilities, the QBO and semiannual oscillation in the equatorial region, and the meridional circulation induced by transient wave forcing in the winter hemisphere. In addition, it would be interesting to examine the difference in the characteristics between the IHC initiated with a Northern Hemisphere stratospheric warming and that with Southern Hemisphere one. Stationary planetary wave activity is stronger in the Northern Hemisphere than in the

Southern Hemisphere which makes a difference in the strength and frequency of the SSW. Subsequently, dominant processes causing the IHC can be different. Moreover, the stratosphere and mesosphere are coupled vertically in each hemisphere. For example, the winter polar vortex breakdown in the Southern Hemisphere largely affects the summer transition in the mesosphere of the hemisphere including the variability of the mesopause height and temperature (Lübken et al., 2017). Such vertical coupling may interfere with the IHC effects.

For these studies, it is particularly important to examine the variability of GWs as an anomaly from the climatology; this will be possible by performing a series of numerical simulations for many years using the GW-permitting GCM validated by observations. The combination of observations and model simulations with high resolution that explicitly treat GW, as demonstrated in the present study, will become a powerful tool for elucidating the dynamics of the IHC and its variability.

Data Availability Statement

The MERRA2 data set is available from Global Modeling and Assimilation Office (2015) and Aura MLS data is available from Schwartz et al. (2020). The processed data from the high-resolution JAGUAR model, JAGUAR-DAS reanalysis, radar observations, and SABER observations are available from Sato et al. (2023) at data archive system in the PANSY radar server with CC-BY 4.0.

References

Alexander, M. J., Geller, M., McLandress, C., Polavarapu, S., Preusse, P., Sassi, F., et al. (2010). Recent developments in gravity-wave effects in climate models and the global distribution of gravity-wave momentum flux from observations and models. *Quarterly Journal of the Royal Meteorological Society*, *136*(650), 1103–1124. https://doi.org/10.1002/qj.637

Amemiya, A., & Sato, K. (2016). A new gravity wave parameterization including three dimensional propagation. *Journal of the Meteorological Society of Japan*, *94*(3), 237–256. https://doi.org/10.2151/jmsj.2016-013

Andrews, D. G., Holton, J. R., & Leovy, C. B. (1987). *Middle atmosphere dynamics* (489 pp.). Academic.

Aso, T., Tsuda, T., & Kato, S. (1979). Meteor radar observations at Kyoto University. *Journal of Atmospheric and Terrestrial Physics*, *41*(5), 517–525. https://doi.org/10.1016/0021-9169(79)90075-8

Batubara, M., Suryana, R., Manik, T., & Sitompul, P. (2011). Kototabang-West Sumatera meteor radar: System design and initial results of a large scale meteor echo. In *2011 6th international conference on telecommunication systems, services, and applications (TSSA)* (pp. 17–21). https://doi.org/10.1109/TSSA.2011.6095399

Baumgarten, G. (2010). Doppler Rayleigh/Mie/Raman lidar for wind and temperature measurements in the middle atmosphere up to 80 km. *Atmospheric Measurement Techniques*, *3*(6), 1509–1518. https://doi.org/10.5194/amt-3-1509-2010

Becker, E., & Fritts, D. C. (2006). Enhanced gravity-wave activity and interhemispheric coupling during the MaCWAVE/MIDAS northern summer program 2002. *Annales Geophysicae*, *24*(4), 1175–1188. https://doi.org/10.5194/angeo-24-1175-2006

Becker, E., & Vadas, S. L. (2018). Secondary gravity waves in the winter mesosphere: Results from a high-resolution global circulation model. *Journal of Geophysical Research: Atmospheres*, *123*(5), 2605–2627. https://doi.org/10.1002/2017JD027460

Briggs, B. H. (1984). The analysis of spaced sensor records by correlation techniques. In *Handbook for MAP* (Vol. 13, pp. 166–186). SCOSTEP Secretariat.

Chandran, A., Garcia, R. R., Collins, R. L., & Chang, L. C. (2013). Secondary planetary waves in the middle and upper atmosphere following the stratospheric sudden warming event of January 2012. *Geophysical Research Letters*, *40*(9), 1861–1867. https://doi.org/10.1002/grl.50373

Charney, J. G., & Drazin, P. G. (1961). Propagation of planetary-scale disturbances from the lower into the upper atmosphere. *Journal of Geophysical Research*, *66*(1), 83–109. https://doi.org/10.1029/JZ066i001p00083

Chu, X., Gardner, C. S., Li, X., & Lin, C. Y.-T. (2022). Vertical transport of sensible heat and meteoric Na by the complete temporal spectrum of gravity waves in the MLT above McMurdo (77.84°S, 166.67°E), Antarctica. *Journal of Geophysical Research: Atmospheres*, *127*(16), e2021JD035728. https://doi.org/10.1029/2021JD035728

Chu, X., Yu, Z. B., Gardner, C. S., Chen, C., & Fong, W. C. (2011). Lidar observations of neutral Fe layers and fast gravity waves in the thermosphere (110–155 km) at McMurdo (77.8°S, 166.7°E), Antarctica. *Geophysical Research Letters*, *38*(23), L23807. https://doi.org/10.1029/2011GL050016

De Wit, R. J., Hibbins, R. E., & Espy, P. J. (2015). The seasonal cycle of gravity wave momentum flux and forcing in the high latitude northern hemisphere mesopause region. *Journal of Atmospheric and Solar-Terrestrial Physics*, *127*, 21–29. https://doi.org/10.1016/j.jastp.2014.10.002

Ern, M., Hoffmann, L., Rhode, S., & Preusse, P. (2022). The mesoscale gravity wave response to the 2022 Tonga volcanic eruption: AIRS and MLS satellite observations and source backtracing. *Geophysical Research Letters*, *49*(10), e2022GL098626. https://doi.org/10.1029/2022GL098626

Ern, M., Preusse, P., Kalisch, S., Kaufmann, M., & Riese, M. (2013). Role of gravity waves in the forcing of quasi two-day waves in the mesosphere: An observational study. *Journal of Geophysical Research: Atmospheres*, *118*(9), 3467–3485. https://doi.org/10.1029/2012JD018208

Ern, M., Trinh, Q. T., Preusse, P., Gille, J. C., Mlynczak, M. G., Russell, J. M., III, & Riese, M. (2018). GRACILE: A comprehensive climatology of atmospheric gravity wave parameters based on satellite limb soundings. *Earth System Science Data*, *10*(2), 857–892. https://doi.org/10.5194/essd-10-857-2018

France, J. A., Randall, C. E., Lieberman, R. S., Harvey, V. L., Eckermann, S. D., Siskind, D. E., et al. (2018). Local and remote planetary wave effects on polar mesospheric clouds in the Northern Hemisphere in 2014. *Journal of Geophysical Research: Atmospheres*, *123*(10), 5149–5162. https://doi.org/10.1029/2017JD028224

Freie Universität Berlin. (2023). The quasi-biennial oscillation (QBO) data serie. Retrieved from https://www.geo.fu-berlin.de/en/met/ag/strat/produkte/qbo/index.html

Fritz, S., & Soules, D. (1972). Planetary variations of stratospheric temperature. *Monthly Weather Review*, *100*(7), 582–589. https://doi.org/10.1175/1520-0493(1972)100,0582:PVOST.2.3.CO;2

Fukao, S., Hashiguchi, H., Yamamoto, M., Tsuda, T., Nakamura, T., Yamamoto, M. K., et al. (2003). Equatorial Atmosphere Radar (EAR): System description and first results. *Radio Science*, *38*(3), 1053. https://doi.org/10.1029/2002RS002767

Fukao, S., Sato, T., Tsuda, T., Kato, S., Wakasugi, K., & Makihara, T. (1985a). The MU radar with an active phased array system: 1. Antenna and power amplifiers. *Radio Science*, *20*(6), 1155–1168. https://doi.org/10.1029/RS020i006p01155

Fukao, S., Tsuda, T., Sato, T., Kato, S., Wakasugi, K., & Makihira, T. (1985b). The MU radar with an active phased array system: 2. In-house equipment. *Radio Science*, *20*(6), 1169–1176. https://doi.org/10.1029/RS020i006p01169

Gelaro, R., McCarty, W., Suárez, M. J., Todling, R., Molod, A., Takacs, L., et al. (2017). The Modern-Era Retrospective Analysis for Research and Applications, version 2 (MERRA-2). *Journal of Climate*, *30*(14), 5419–5454. https://doi.org/10.1175/JCLI-D-16-0758.1

Global Modeling and Assimilation Office (GMAO). (2015). MERRA-2 inst3_3d_asm_Np: 3d,3-hourly, instantaneous, pressure-level, assimilation, assimilated meteorological fields V5.12.4 [Dataset]. Goddard Earth Sciences Data and Information Services Center (GES DISC). https://doi.org/10.5067/QBZ6MG944HW0

Gregory, J. B., Meek, C. E., & Manson, A. H. (1981). *An assessment of winds data (60–110 km) obtained in realtime from a medium frequency radar*. Report No. 6. Institute of Space and Atmospheric Studies, University of Saskatchewan.

Gumbel, J., & Karlsson, B. (2011). Intra- and inter-hemispheric coupling effects on the polar summer mesosphere. *Geophysical Research Letters*, *38*(14), L14804. https://doi.org/10.1029/2011GL047968

Hall, C. M. (2001). The Ramfjordmoen MF radar (69°N, 1°E): Application development 1990–2000. *Journal of Atmospheric and Solar-Terrestrial Physics*, *63*(2–3), 171–179. https://doi.org/10.1016/s1364-6826(00)00144-9

Hall, C. M., Aso, T., & Tsutsumi, M. (2002). An examination of high latitude upper mesosphere dynamic stability using the Nippon/Norway Svalbard Meteor Radar. *Geophysical Research Letters*, *29*(8), 1280. https://doi.org/10.1029/2001GL014229

Hashimoto, T., Saito, A., Nishimura, K., Tsutsumi, M., Sato, K., & Sato, T. (2019). First incoherent scatter measurements and adaptive suppression of field-aligned irregularities by the PANSY radar at Syowa Station, Antarctic. *Journal of Atmospheric and Oceanic Technology*, *36*(9), 1881–1888. https://doi.org/10.1175/jtech-d-18-0175.1

Hersbach, H., Bell, B., Berrisford, P., Hirahara, S., Horányi, A., Muñoz-Sabater, J., et al. (2020). The ERA5 global reanalysis. *Quarterly Journal of the Royal Meteorological Society*, *146*(730), 1999–2049. https://doi.org/10.1002/qj.3803

Hocking, W. K. (1999). Temperatures using radar-meteor decay times. *Geophysical Research Letters*, *26*(21), 3297–3300. https://doi.org/10.1029/1999gl003618

Hocking, W. K. (2005). A new approach to momentum flux determinations using SKiYMET meteor radars. *Annales Geophysicae*, *23*(7), 2433–2439. https://doi.org/10.5194/angeo-23-2433-2005

Hocking, W. K., Fuller, B., & Vandepeer, B. (2001). Real-time determination of meteor related parameters utilizing modern digital technology. *Journal of Atmospheric and Solar-Terrestrial Physics*, *63*(2–3), 155–169. https://doi.org/10.1016/s1364-6826(00)00138-3

Hocking, W. K., & Hocking, A. (2002). Temperature tides determined with meteor radar. *Annales Geophysicae*, *20*(9), 1447–1467. https://doi.org/10.5194/angeo-20-1447-2002

Hocking, W. K., Röttger, J., Palmer, R. D., Sato, T., & Chilson, P. B. (2016). *Atmospheric radar: Application and science of MST radars in the Earth's mesosphere, stratosphere, troposphere and weakly ionized regions* (838 pp.). Cambridge University Press. ISBN 978-1-107-14746-1.

Holdsworth, D. A., Reid, I. M., & Cervera, M. A. (2004). The Buckland Park all-sky interferometric meteor radar—Description and first results. *Radio Science*, *39*(5), RS5009. https://doi.org/10.1029/2003RS003014

Hysell, D. L., Chau, J. L., & Milla, M. A. (2013). The Jicamarca phased-array radar. In *2013 IEEE international symposium on phased array systems and technology* (pp. 669–675). https://doi.org/10.1109/ARRAY.2013.6731910

Jaen, J., Renkwitz, T., Chau, J. L., He, M., Hoffmann, P., Yamazaki, Y., et al. (2022). Long-term studies of mesosphere and lower-thermosphere summer length definitions based on mean zonal wind features observed for more than one solar cycle at middle and high latitudes in the Northern Hemisphere. *Annales Geophysicae*, *40*(1), 23–35. https://doi.org/10.5194/angeo-40-23-2022

Jarvis, M. J., Jones, G. O. L., & Jenkins, B. (1999). New initiatives in observing the Antarctic mesosphere. *Advances in Space Research*, *24*(5), 611–619. https://doi.org/10.1016/S0273-1177(99)00479-2

Jin, H., Miyoshi, Y., Fujiwara, H., Shinagawa, H., Terada, K., Terada, N., et al. (2011). Vertical connection from the tropospheric activities to the ionospheric longitudinal structure simulated by a new Earth's whole atmosphere-ionosphere coupled model. *Journal of Geophysical Research*, *116*(A1), A01316. https://doi.org/10.1029/2010JA015925

Kaiser, T. R. (1953). Radio echo studies of meteor ionization. *Philosophical Magazine*, *2*(8), 495–544. https://doi.org/10.1080/00018735300101282

Karlsson, B., Körnich, H., & Gumbel, J. (2007). Evidence for interhemispheric stratosphere-mesosphere coupling derived from noctilucent cloud properties. *Geophysical Research Letters*, *34*(16), L16806. https://doi.org/10.1029/2007GL030282

Karlsson, B., McLandress, C., & Shepherd, T. G. (2009). Inter-hemispheric mesospheric coupling in a comprehensive middle atmosphere model. *Journal of Atmospheric and Solar-Terrestrial Physics*, *71*(3–4), 518–530. https://doi.org/10.1016/j.jastp.2008.08.006

Karlsson, B., Randall, C. E., Benze, S., Mills, M., Harvey, V. L., Bailey, S. M., & Russell, J. M. (2009). Intra-seasonal variability of polar mesospheric clouds due to inter-hemispheric coupling. *Geophysical Research Letters*, *36*(20), L20802. https://doi.org/10.1029/2009GL040348

Körnich, H., & Becker, E. (2010). A simple model for the interhemispheric coupling of the middle atmosphere circulation. *Advances in Space Research*, *45*(5), 661–668. https://doi.org/10.1016/j.asr.2009.11.001

Koshin, D., Kohma, M., & Sato, K. (2022). Characteristics of the intraseasonal oscillation in the equatorial mesosphere and lower thermosphere region revealed by satellite observation and global analysis by the JAGUAR data assimilation system. *Journal of Geophysical Research: Atmospheres*, *127*(16), e2022JD036816. https://doi.org/10.1029/2022JD036816

Koshin, D., Sato, K., Kohma, M., & Watanabe, S. (2022). An update on the 4D-LETKF data assimilation system for the whole neutral atmosphere. *Geoscientific Model Development*, *15*(5), 2293–2022. https://doi.org/10.5194/gmd-15-2293-2022

Koshin, D., Sato, K., Miyazaki, K., & Watanabe, S. (2020). An ensemble Kalman filter data assimilation system for the whole neutral atmosphere. *Geoscientific Model Development*, *13*(7), 3145–3177. https://doi.org/10.5194/gmd-13-3145-2020

Kristoffersen, S., Ward, W. E., Brown, S., & Drummond, J. R. (2013). Calibration and validation of the advanced E-Region Wind Interferometer. *Atmospheric Measurement Techniques*, *6*(7), 1–16. https://doi.org/10.5194/amt-6-1761-2013

Labitzke, K. (1972). Temperature changes in the mesosphere and stratosphere connected with circulation changes in winter. *Journal of the Atmospheric Sciences*, *29*(4), 756–766. https://doi.org/10.1175/1520-0469(1972)029<0756:tcitma>2.0.co;2

Latteck, R., Singer, W., Rapp, M., Vandepeer, B., Renkwitz, T., Zecha, M., & Stober, G. (2012). MAARSY: The new MST radar on Andøya—System description and first results. *Radio Science*, *47*, 1–18. https://doi.org/10.1029/2011rs004775

Lawrence, Z. D., Perlwitz, J., Butler, A. H., Manney, G. L., Newman, P. A., Lee, S. H., & Nash, E. R. (2020). The remarkably strong Arctic stratospheric polar vortex of winter 2020: Links to record-breaking Arctic Oscillation and ozone loss. *Journal of Geophysical Research: Atmospheres*, *125*(22), e2020JD033271. https://doi.org/10.1029/2020JD033271

Lee, K., Kudeki, E., Reyes, P. M., Lehmacher, G. A., & Milla, M. (2019). Mesospheric wind estimation with the Jicamarca MST radar using spectral mainlobe identification. *Radio Science*, *54*(12), 1222–1239. https://doi.org/10.1029/2019RS006892

Lieberman, R. S., France, J., Ortland, D. A., & Eckermann, S. D. (2021). The role of inertial instability in cross-hemispheric coupling. *Journal of the Atmospheric Sciences*, *78*(4), 1113–1127. https://doi.org/10.1175/JAS-D-20-0119.1

Limpasuvan, V., Orsolini, Y. J., Chandran, A., Garcia, R. R., & Smith, A. K. (2016). On the composite response of the MLT to major sudden stratospheric warming events with elevated stratopause. *Journal of Geophysical Research: Atmospheres*, *121*(9), 4518–4537. https://doi.org/10.1002/2015JD024401

Liu, H.-L., McInerney, J. M., Santos, S., Lauritzen, P. H., Taylor, M. A., & Pedatella, N. M. (2014). Gravity waves simulated by high-resolution Whole Atmosphere Community Climate Model. *Geophysical Research Letters*, *41*(24), 9106–9112. https://doi.org/10.1002/2014GL062468

Livesey, N. J., Read, W. G., Wagner, P. A., Froidevaux, L., Santee, M. L., Schwartz, M. J., & Lay, R. R. (2022). *Earth Observing System (EOS) aura Microwave Limb Sounder (MLS) version 5.0x level 2 and 3 data quality and description document Version 5.0–1.1a* (Tech. Rep.). Jet Propulsion Laboratory, California Institute of Technology. Retrieved from https://mls.jpl.nasa.gov/data/v5-0_data_quality_document.pdf

Lübken, F., Latteck, R., Becker, E., Höffner, J., & Murphy, D. (2017). Using polar mesosphere summer echoes and stratospheric/mesospheric winds to explain summer mesopause jumps in Antarctica. *Journal of Atmospheric and Solar-Terrestrial Physics*, *162*, 106–115. https://doi.org/10.1016/j.jastp.2016.06.008

McCormack, J. P., Harvey, V. L., Pedatella, N., Koshin, D., Sato, K., Coy, L., et al. (2021). Intercomparison of middle atmospheric meteorological analyses for the Northern Hemisphere winter 2009–2010. *Atmospheric Chemistry and Physics*, *21*, 17577–17605. https://doi.org/10.5194/acp-21-17577-2021

Medvedeva, I. V., Semenov, A. I., Perminov, V. I., Beletsky, A. B., & Tatarnikov, A. V. (2014). Comparison of ground-based OH temperature data measured at Irkutsk (52°N, 103°E) and Zvenigorod (56°N, 37°E) stations with Aura MLS v3.3. *Acta Geophysica*, *62*(2), 340–349. https://doi.org/10.2478/s11600-013-0161-x

Miyoshi, T., & Yamane, S. (2007). Local ensemble transform Kalman filtering with an AGCM at a T159/L48 resolution. *Monthly Weather Review*, *135*(11), 3841–3861. https://doi.org/10.1175/2007MWR1873.1

Morris, R. J., Murphy, D. J., Reid, I. M., Holdsworth, D. A., & Vincent, R. A. (2004). First polar mesosphere summer echoes observed at Davis, Antarctica (68.6°S). *Geophysical Research Letters*, *31*(16), L16111. https://doi.org/10.1029/2004GL020352

Murphy, D. J. (2017). *Davis 33MHz meteor detection radar winds, Ver. 1*. Australian Antarctic Data Centre. Retrieved from https://data.aad.gov.au/metadata/records/Davis_33MHz_Meteor_Radar

Murphy, D. J., Alexander, S. P., & Vincent, R. A. (2012). Interhemispheric dynamical coupling to the southern mesosphere and lower thermosphere. *Journal of Geophysical Research*, *117*(D8), D08114. https://doi.org/10.1029/2011JD016865

Murphy, D. J., & Vincent, R. A. (2000). Amplitude enhancements in Antarctic MF radar echoes. *Journal of Geophysical Research*, *105*(D21), 26683–26693. https://doi.org/10.1029/2000jd900510

Naren Athreyas, K., Garcia, R., & Chandran, A. (2022). Inter-hemispheric coupling during sudden stratospheric warming events with elevated stratopause. *Journal of Geophysical Research: Atmospheres*, *127*(1), e2020JD033761. https://doi.org/10.1029/2020JD033761

Nozawa, S., Kawahara, T. D., Saito, N., Hall, C. M., Tsuda, T. T., Kawabata, T., et al. (2014). Variations of the neutral temperature and sodium density between 80 and 107 km above Tromsø during the winter of 2010–2011 by a new solid-state sodium lidar. *Journal of Geophysical Research: Space Physics*, *119*(1), 441–451. https://doi.org/10.1002/2013JA019520

Okui, H., Sato, K., Koshin, D., & Watanabe, S. (2021). Formation of a mesospheric inversion layer and the subsequent elevated stratopause associated with the major stratospheric sudden warming in 2018/19. *Journal of Geophysical Research: Atmospheres*, *126*(18), e2021JD034681. https://doi.org/10.1029/2021JD034681

Orsolini, Y. J., Limpasuvan, V., & Leovy, C. B. (1997). The tropical stratopause in the UKMO stratospheric analysis: Evidence for a 2-day wave and inertial circulations. *Quarterly Journal of the Royal Meteorological Society*, *123*(542), 1707–1724. https://doi.org/10.1002/qj.49712354212

Pendlebury, D. (2012). A simulation of the quasi-two-day wave and its effect on variability of summertime mesopause temperatures. *Journal of Atmospheric and Solar-Terrestrial Physics*, *80*, 138–151. https://doi.org/10.1016/j.jastp.2012.01.006

Plumb, R. A. (1983). Baroclinic instability of the summer mesosphere: A mechanism for the quasi-two-day wave? *Journal of the Atmospheric Sciences*, *40*(1), 262–270. https://doi.org/10.1175/1520-0469(1983)040<0262:biotsm>2.0.co;2

Plumb, R. A. (2002). Stratospheric transport. *Journal of the Meteorological Society of Japan*, *80*(4B), 793–809. https://doi.org/10.2151/jmsj.80.793

Qiao, L., Chen, G., Zhang, S., Yao, Q., Gong, W., Su, M., et al. (2020). Wuhan MST radar: Technical features and validation of wind observations. *Atmospheric Measurement Technique*, *13*(10), 5697–5713. https://doi.org/10.5194/amt-13-5697-2020

Reid, I. M. (2015). MF and HF radar techniques for investigating the dynamics and structure of the 50 to 110 km height region: A review. *Progress in Earth and Planetary Science*, *2*, 1–34. https://doi.org/10.1186/s40645-015-0060-7

Reid, I. M., & Vincent, R. A. (1987). Measurements of mesospheric gravity wave momentum fluxes and mean flow accelerations at Adelaide, Australia. *Journal of Atmospheric and Terrestrial Physics*, *49*(5), 443–460. https://doi.org/10.1016/0021-9169(87)90039-0

Remsberg, E. E., Marshall, B. T., Garcia-Comas, M., Krueger, D., Lingenfelser, G. S., Martin-Torres, J., et al. (2008). Assessment of the quality of the retrieved temperature versus pressure profiles in the middle atmosphere from TIMED/SABER. *Journal of Geophysical Research*, *113*(D17), D17101. https://doi.org/10.1029/2008JD010013

Renkwitz, T., Tsutsumi, M., Laskar, F. I., Chau, J. L., & Latteck, R. (2018). On the role of anisotropic MF/HF scattering in mesospheric wind estimation. *Earth, Planets and Space*, *70*, 1–16. https://doi.org/10.1186/s40623-018-0927-0

Rishbeth, H., & Williams, P. J. S. (1985). The EISCAT ionospheric radar-The system and its early results. *Quarterly Journal of the Royal Astronomical Society*, *26*, 478–512.

Sato, K. (1990). Vertical wind disturbances in the troposphere and lower stratosphere observed by the MU radar. *Journal of the Atmospheric Sciences*, *47*(23), 2803–2817. https://doi.org/10.1175/1520-0469(1990)047<2803:VWDITT>2.0.CO;2

Sato, K., Kohma, M., Tsutsumi, M., & Sato, T. (2017). Frequency spectra and vertical profiles of wind fluctuations in the summer Antarctic mesosphere revealed by MST radar observations. *Journal of Geophysical Research: Atmospheres*, *122*(1), 3–19. https://doi.org/10.1002/2016JD025834

Sato, K., & Nomoto, M. (2015). Gravity wave–induced anomalous potential vorticity gradient generating planetary waves in the winter mesosphere. *Journal of the Atmospheric Sciences*, *72*(9), 3609–3624. https://doi.org/10.1175/JAS-D-15-0046.1

Sato, K., Tateno, S., Watanabe, S., & Kawatani, Y. (2012). Gravity wave characteristics in the Southern Hemisphere revealed by a high-resolution middle-atmosphere general circulation model. *Journal of the Atmospheric Sciences*, *69*(4), 1378–1396. https://doi.org/10.1175/JAS-D-11-0101.1

Sato, K., Tomikawa, Y., Kohma, M., Yasui, R., Koshin, D., Okui, H., et al. (2023). The processed data from the high-resolution JAGUAR model, JAGUAR-DAS reanalysis, radar observations, and SABER observations for "Interhemispheric Coupling Study by Observations and Modelling (ICSOM): Concept, campaigns, and initial results" [Dataset]. ICSOM. https://pansy.eps.s.u-tokyo.ac.jp/archive_data/Sato_etal_ICSOM/

Sato, K., Tsutsumi, M., Sato, T., Nakamura, T., Saito, A., Tomikawa, Y., et al. (2014). Program of the Antarctic Syowa MST/IS radar (PANSY). *Journal of Atmospheric and Solar-Terrestrial Physics*, *118A*, 2–15. https://doi.org/10.1016/j.jastp.2013.08.022

Sato, K., Watanabe, S., Kawatani, Y., Tomikawa, Y., Miyazaki, K., & Takahashi, M. (2009). On the origins of mesospheric gravity waves. *Geophysical Research Letters*, *36*(19), L19801. https://doi.org/10.1029/2009GL039908

Sato, K., Yasui, R., & Miyoshi, Y. (2018). The momentum budget in the stratosphere, mesosphere, and lower thermosphere. Part I: Contributions of different wave types and in situ generation of Rossby waves. *Journal of the Atmospheric Sciences*, *75*(10), 3613–3633. https://doi.org/10.1175/JAS-D-17-0336.1

Schwartz, M., Livesey, N., & Read, W. (2020). *MLS/aura level 2 temperature V005*. Goddard Earth Sciences Data and Information Services Center (GES DISC). https://doi.org/10.5067/Aura/MLS/DATA2520

Schwartz, M. J., Lambert, A., Manney, G. L., Read, W. G., Livesey, N. J., Froidevaux, L., et al. (2008). Validation of the Aura Microwave Limb Sounder temperature and geopotential height measurements. *Journal of Geophysical Research*, *113*(D15), D15S11. https://doi.org/10.1029/2007JD008783

Senf, F., & Achatz, U. (2011). On the impact of middle-atmosphere thermal tides on the propagation and dissipation of gravity waves. *Journal of Geophysical Research*, *116*(D24), D24110. https://doi.org/10.1029/2011jd015794

Shiokawa, K., Katoh, Y., Satoh, M., Ejiri, M. K., Ogawa, T., Nakamura, T., et al. (1999). Development of optical Mesosphere Thermosphere imagers (OMTI). *Earth, Planets and Space*, *51*(7–8), 887–896. https://doi.org/10.1186/bf03353247

Siskind, D. E., & McCormack, J. P. (2014). Summer mesospheric warmings and the quasi 2 day wave. *Geophysical Research Letters*, *41*, 717–722. https://doi.org/10.1002/2013GL058875

Slater, K., Stevens, A. D., Pearmain, S. A. M., Eccles, D., Hall, A. J., Bennett, R. G. T., et al. (1991). *Overview of the MST radar system at Aberystwyth* (p. 479). Solar-Terrestrial Energy Program.

Smith, A. K., Garcia, R. R., Marsh, D. R., Kinnison, D. E., & Richter, J. H. (2010). Simulations of the response of mesospheric circulation and temperature to the Antarctic ozone hole. *Geophysical Research Letters*, *37*(22), L22803. https://doi.org/10.1029/2010GL045255

Smith, A. K., Pedatella, N. M., & Bardeen, C. G. (2022). Global middle-atmosphere response to winter stratospheric variability in SABER and MLS mean temperature. *Journal of the Atmospheric Sciences*, *79*(6), 1727–1741. https://doi.org/10.1175/JAS-D-21-0259.1

Smith, A. K., Pedatella, N. M., & Mullen, Z. K. (2020). Interhemispheric coupling mechanisms in the middle atmosphere of WACCM6. *Journal of the Atmospheric Sciences*, *77*(3), 1101–1118. https://doi.org/10.1175/JAS-D-19-0253.1

Stone, K. A., Solomon, S., Kinnison, D. E., & Mills, M. J. (2021). On recent large Antarctic ozone holes and ozone recovery metrics. *Geophysical Research Letters*, *48*(22), e2021GL095232. https://doi.org/10.1029/2021GL095232

Swadley, S. D., Poe, G. A., Bell, W., Hong, Y., Kunkee, D. B., McDermid, I. S., & Leblanc, T. (2008). Analysis and characterization of the SSMIS upper atmosphere sounding channel measurements. *IEEE Transactions on Geoscience and Remote Sensing*, *46*(4), 962–983. https://doi.org/10.1109/TGRS.2008.916980

Tan, B., Chu, X., Liu, H.-L., Yamashita, C., & Russell, J. M. (2012). Zonal-mean global teleconnection from 15 to 110 km derived from SABER and WACCM. *Journal of Geophysical Research*, *117*(D10), D10106. https://doi.org/10.1029/2011JD016750

Thurairajah, B., Bailey, S. M., Cullens, C. Y., Hervig, M. E., & Russell, J. M. (2014). Gravity wave activity during recent stratospheric sudden warming events from SOFIE temperature measurements. *Journal of Geophysical Research: Atmospheres*, *119*(13), 8091–8103. https://doi.org/10.1002/2014JD021763

Thurairajah, B., Collins, R. L., Harvey, V. L., Lieberman, R. S., Gerding, M., Mizutani, K., & Livingston, J. M. (2010). Gravity wave activity in the arctic stratosphere and mesosphere during the 2007–2008 and 2008–2009 stratospheric sudden warming events. *Journal of Geophysical Research*, *115*, D00N06. https://doi.org/10.1029/2010JD014125

Thurairajah, B., Collins, R. L., Harvey, V. L., Lieberman, R. S., & Mizutani, K. (2010). Rayleigh lidar observations of reduced gravity wave activity during the formation of an elevated stratopause in 2004 at Chatanika, Alaska (65°N, 147°W). *Journal of Geophysical Research*, *115*(D13), D13109. https://doi.org/10.1029/2009JD013036

Tian, Y., & Lü, D. (2017). Comparison of Beijing MST radar and radiosonde horizontal wind measurements. *Advances in Atmospheric Sciences*, *34*(1), 39–53. https://doi.org/10.1007/s00376-016-6129-4

Tomikawa, Y., Sato, K., Watanabe, S., Kawatani, Y., Miyazaki, K., & Takahashi, M. (2012). Growth of planetary waves and the formation of an elevated stratopause after a major stratospheric sudden warming in a T213L256 GCM. *Journal of Geophysical Research*, *117*(D16), D16101. https://doi.org/10.1029/2011JD017243

Triplett, C. C., Li, J., Collins, R. L., Lehmacher, G. A., Barjatya, A., Fritts, D. C., et al. (2018). Observations of reduced turbulence and wave activity in the Arctic middle atmosphere following the January 2015 sudden stratospheric warming. *Journal of Geophysical Research: Atmospheres*, *123*(23), 13259–13276. https://doi.org/10.1029/2018JD028788

Tsuchiya, S., Shiokawa, K., Fujinami, H., Otsuka, Y., Nakamura, T., & Yamamoto, M. (2018). Statistical analysis of the phase velocity distribution of mesospheric and ionospheric waves observed in airglow images over a 16-year period: Comparison between Rikubetsu and Shigaraki, Japan. *Journal of Geophysical Research: Space Physics*, *123*(8), 6930–6947. https://doi.org/10.1029/2018JA025585

Tsuda, T., Murayama, Y., Yamamoto, M., Kato, S., & Fukao, S. (1990). Seasonal-variation of momentum flux in the mesosphere observed with the MU radar. *Geophysical Research Letters*, *17*(6), 725–728. https://doi.org/10.1029/GL017i006p00725

Tsutsumi, M., Aso, T., & Ejiri, M. (2001). Initial results of Syowa MF radar observations in Antarctica. *Advances in Polar Upper Atmosphere Research*, *15*, 103–116.

Tsutsumi, M., Tsuda, T., Nakamura, T., & Fukao, S. (1994). Temperature fluctuations near the mesopause inferred from meteor observations with the middle and upper atmosphere radar. *Radio Science*, *29*(3), 599–610. https://doi.org/10.1029/93rs03590

Tsutsumi, M., Tsuda, T., Nakamura, T., & Fukao, S. (1996). Wind velocity and temperature fluctuations due to a 2-day wave observed with radio meteor echoes. *Journal of Geophysical Research*, *101*(D5), 9425–9432. https://doi.org/10.1029/95jd03579

Vadas, S. L., Zhao, J., Chu, X., & Becker, E. (2018). The excitation of secondary gravity waves from local body forces: Theory and observation. *Journal of Geophysical Research: Atmospheres*, *123*(17), 9296–9325. https://doi.org/10.1029/2017JD027970

VanZandt, T. E. (1982). A universal spectrum of buoyancy waves in the atmosphere. *Geophysical Research Letters*, *9*(5), 575–578. https://doi.org/10.1029/GL009i005p00575

Vincent, R. A. (2015). The dynamics of the mesosphere and lower thermosphere: A brief review. *Progress in Earth and Planetary Science*, *2*, 1–13. https://doi.org/10.1186/s40645-015-0035-8

Vincent, R. A., & Reid, I. M. (1983). HF Doppler measurements of mesospheric gravity wave momentum fluxes. *Journal of the Atmospheric Sciences*, *40*(5), 1321–1333. https://doi.org/10.1175/1520-0469(1983)040<1321:hdmomg>2.0.co;2

Wang, Y., Li, G., Ning, B., Yang, S., Sun, W., & Yu, Y. (2019). All-sky interferometric meteor radar observations of zonal structure and drifts of low-latitude ionospheric E region irregularities. *Earth and Space Science*, *6*(12), 2653–2662. https://doi.org/10.1029/2019EA000884

Wannberg, G., Wolf, I., Vanhainen, L. G., Koskenniemi, K., Röttger, J., Postila, M., et al. (1997). The EISCAT Svalbard radar: A case study in modern incoherent scatter radar system design. *Radio Science*, *32*(6), 2283–2307. https://doi.org/10.1029/97RS01803

Watanabe, S., Kawatani, Y., Tomikawa, Y., Miyazaki, K., Takahashi, M., & Sato, K. (2008). General aspects of a T213L256 middle atmosphere general circulation model. *Journal of Geophysical Research*, *113*(D12), D12110. https://doi.org/10.1029/2008JD010026

Watanabe, S., Koshin, D., Noguchi, S., & Sato, K. (2022). Gravity wave morphology during the 2018 sudden stratospheric warming simulated by a whole neutral atmosphere general circulation model. *Journal of Geophysical Research: Atmospheres*, *127*(19), e2022JD036718. https://doi.org/10.1029/2022JD036718

Watanabe, S., & Miyahara, S. (2009). Quantification of the gravity wave forcing of the migrating diurnal tide in a gravity wave–resolving general circulation model. *Journal of Geophysical Research*, *114*(D7), D07110. https://doi.org/10.1029/2008JD011218

Watanabe, S., Tomikawa, Y., Sato, K., Kawatani, Y., Miyazaki, K., & Takahashi, M. (2009). Simulation of the eastward 4-day wave in the Antarctic winter mesosphere using a gravity wave resolving general circulation model. *Journal of Geophysical Research*, *114*(D16), D16111. https://doi.org/10.1029/2008JD011636

Waters, J. W., Froidevaux, L., Harwood, R. S., Jarnot, R. F., Pickett, H. M., Read, W. G., et al. (2006). The Earth Observing System Microwave Limb Sounder (EOS MLS) on the Aura satellite. *IEEE Transactions on Geoscience and Remote Sensing*, *44*(5), 1075–1092. https://doi.org/10.1109/TGRS.2006.873771

Yamashita, C., Liu, H.-L., & Chu, X. (2010). Gravity wave variations during the 2009 stratospheric sudden warming as revealed by ECMWF-T799 and observations. *Geophysical Research Letters*, *37*, L22806. https://doi.org/10.1029/2010GL045437

Yasui, R., Sato, K., & Miyoshi, Y. (2018). The momentum budget in the stratosphere, mesosphere, and lower thermosphere. Part II: The in situ generation of gravity waves. *Journal of the Atmospheric Sciences*, *75*(10), 3635–3651. https://doi.org/10.1175/JAS-D-17-0337.1

Yasui, R., Sato, K., & Miyoshi, Y. (2021). Roles of Rossby waves, Rossby–gravity waves, and gravity waves generated in the middle atmosphere for interhemispheric coupling. *Journal of the Atmospheric Sciences*, *78*, 3867–3888. https://doi.org/10.1175/JAS-D-21-0045.1

Yasui, R., Sato, K., & Tsutsumi, M. (2016). Seasonal and interannual variation of mesospheric gravity waves based on MF radar observations over 15 years at Syowa Station in the Antarctic. *SOLA*, *12*(0), 46–50. https://doi.org/10.2151/sola.2016-010

Yu, Y., Wan, W., Ning, B., Liu, L., Wang, Z., Hu, L., & Ren, Z. (2013). Tidal wind mapping from observations of a meteor radar chain in December 2011. *Journal of Geophysical Research: Space Physics*, *118*(5), 2321–2332. https://doi.org/10.1029/2012JA017976